University of California, Berkeley

Berkeley, CA 94720, USA

Technical Report No. (EPS/2014/000)

A stochastic hydraulic conductivity model for weathered bedrock.

Author:
Michail Vrettas, PhD

Supervisor:
Prof. Inez Fung

February 16, 2015

Keywords:

Abstract

Preferential flow through weathered bedrock leads to rapid rise of the water table after the first rainstorms and significant storage (also known as "rock moisture") in the fractures. We present a novel stochastic model of hydraulic conductivity that captures the preferential flow and is easy to implement in global climate models. To mimic the naturally varying heterogeneity of the subsurface, the model represents the hydraulic conductivity as a product of the effective saturation and a background hydraulic conductivity (K_{bkg}), assumed to be log-normally distributed. The mean of the background K_{bkg} decreases monotonically with depth, while its variance reduces with the effective saturation. Model parameters are derived by assimilating into Richards' equation 30-minute observations of precipitation [mm] and water table depths [m] from a steep hill-slope in Northern California. The results show that the observed rapid penetration of precipitation and the fast rise of the water table, after the first winter rains, is well captured with the stochastic model and not with the standard van Genuchten model of hydraulic conductivity. Furthermore, storage of moisture in the soil mantle and weathered bedrock is smaller, implying greater runoff, with the new stochastic model.

1 Introduction

The soil column below an organic mantle is heterogeneous. Typically the organic–rich 'A' horizon is underlain by a 'B' horizon with minimal organic content and higher clay content or other products of weathering. In landscapes developed on bedrock the 'B' horizon rests on weathered bedrock, which can range from an intensively altered soil–like material that still retains a relict rock structure (saprolite) to weathered (fractured) bedrock that eventually grades into fresh bedrock. The saprolite ranges from absent to 10's of meters thick and the weathered bedrock zone may be thin or range up to 10's m or more. Saprolite can be more or less hydraulically conductive (depending on rock type) and mediate the passage of water to still greater depths. It is widespread in the tropics and mid–latitudes, and is abundant especially in the Piedmont formation in the Eastern U.S. Saprolite contains preferential flow paths (including fractures) where plant roots are found. The paths could provide rapid transmission of water as well as hold non–negligible amounts of water accessible to plants. The saturated hydraulic conductivity of saprolite is highly variable and could be as high as ~ 200 m/y [55], comparable to that of sandy clay loam. Between the saprolite layer and the fresh bedrock is weathered bedrock where fractures are often found. During downpours water can penetrate rapidly, via fractures and the water table fluctuates with rain events even when the soil, saprolite and upper part of the weathered bedrock zone is not saturated [44, 30].

At a research site dubbed "Rivendell", on a steep hill–slope in the Angelo Coast Range Reserve in the Eel River Watershed in Northern California, the nearly five years of high–frequency ($\sim$ every 30 minutes) data shows that the water tables more than 18 meters below the surface can respond in less than 8 hours to the first rains, suggesting very fast flow through macro–pores and fractured rock (e.g. Figure 1). Not quite as quickly as the water table rises after a heavy rain the elevated water level recedes, contributing to downslope flow and streamflow. This "quick recording" and "slow forgetting" of the water table has been noted in two New Jersey wells by [12]. "Rock moisture", a term we use for the moisture between the thin top organic mantle and the water table, is very dynamic, and comprises about 30% of the total moisture in the column above the water table [44].

This dynamic flow through the upper soil and weathered bedrock builds a perched water table that eventually drains to adjacent channels, supporting river base–flow. It reduces shallow water storage for the dry season (due to water by–passing the near surface layers), and yet leaves behind remnants of water in the saprolite and weathered rock matrix and rock fractures (i.e. "rock moisture") that is accessible by roots. The seasonal recharge of this moisture is from above, not from capillarity from a lower groundwater table which will be insignificant in the open fractures of the weathered bedrock.

There is a large body of hydrogeology literature on flow and contaminant transport through fractured porous media, see discussion in [1, 48]. In sophisticated dual–permeability models [17, 50, 49], fracture networks are described in detail according to their size, density, orientation and connectivity patterns, see Figure (1).

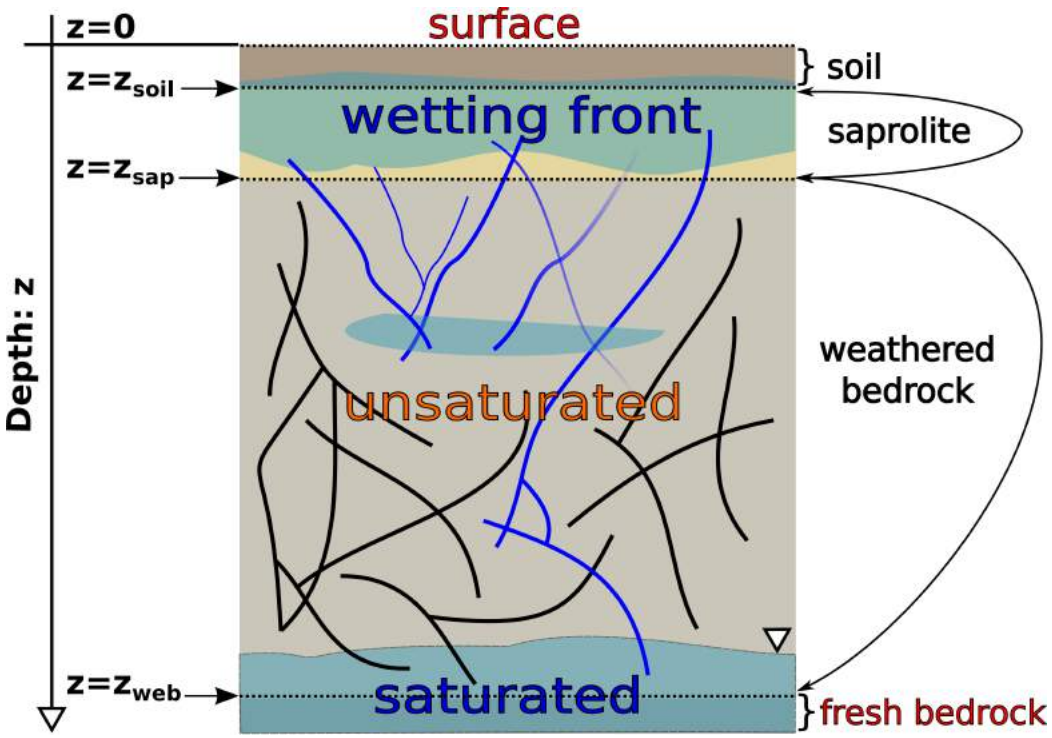

Figure 1: Simplified schematic illustration of the assumed underground layers (spatial domain), with depth values z increasing downwards. Fractures are indicated by curved lines, while blue color denotes saturation. Occasionally, pockets of saturated soil can be formed in the weathered bedrock (blue shaded area) as a result of preferential flows that would allow the water to move faster. The water table is marked by the inverse triangle (bottom right corner). Red labeled layers (i.e. surface and fresh bedrock) are not included in our model.

Yet the lack of relevant global datasets on the geology and hydraulic properties of the heterogeneous subsurface below the soil layer has necessitated many assumptions in the representation of subsurface hydrology in climate models. For example, the hydrologically active soil column in the Community Land Model CLM 4.5 in the NCAR global climate model has a globally uniform thickness of 3.8m [23]. The hydraulic conductivity of the soil column is a combination of a mineral component that depends on soil texture and an organic component [33]. CLM 4.5 includes an aquifer directly under the soil column [23, 32], with the exchange between the soil layer and the aquifer by capillary action. The parameters in the algorithms were chosen to yield reasonable surface soil moisture and annual climatologic stream flow.

1.1 Main Ideas & Outline

In this paper we develop a new model of hydraulic conductivity that captures preferential flow and yet is simple enough to be implemented in global climate models. The algorithm is applied to data from "Well–10" and it shows that it captures the fast rise of the water table after the first winter rains with great accuracy. The main ideas we introduce in this work are as follows:

1. First, in order to mimic the heterogeneity that occurs naturally in the underground the new model follows a stochastic approach by modeling the hydraulic conductivity with a Log–Normal distribution.

2. Secondly, to make our approach more generic we allow the mean and the variance of the Log–Normal distribution to have specific parameterizations, thus making the new algorithm more flexible and adaptable to different locations.

3. Lastly we explore various parameterizations of the porosity profiles, that can also be linked to locations with different geological morphologies.

The rest of the paper is outlined as follows. In Section (2), the governing equations along with initial and boundary conditions are defined. The new stochastic hydraulic conductivity model is introduced in Section (3), while details about the numerical approach applied to solve the problem are given in Section (4). Furthermore, the experimental setup along with the results of our extensive simulations are presented in Section (5). Finally, the paper concludes in Section (6), with a discussion about the findings of this current work, in addition to limitations and possible future extensions.

2 Governing Equations

In environmental sciences a popular approach when modeling the flow of underground water in unsaturated soils is the well known Richards' equation (RE) [39]. It is derived by applying the *continuity requirement* to Darcy's law, which describes the (laminar) flow of fluids through saturated porous mediums. This equation appears in several forms, with more predominant the soil moisture (θ-based) and the pressure head (ψ-based) [6].

Even though intuitively it is easier to think in terms of water content, when both saturated and unsaturated regions in the underground are of interest it is more desirable to choose the pressure (or matric) head ψ, rather than the soil moisture content θ, as the dependent variable [18]. This is because at full saturation the soil moisture does not change, but the pressure head still varies in saturated layers [6, 41]. Furthermore, as [61] have demonstrated, when the water table exists inside the model domain, solving the θ-based RE numerically produces deficiencies in the computation of water content θ (due to truncation errors), therefore affecting directly the vertical soil moisture distribution, that cannot be removed by simply reducing the spatial grid size.

Another advantage of choosing the pressure head form of RE is that it provides a state variable that is always continuous in space, regardless of soil inhomogeneities. The one dimensional pressure head $\psi(z,t)$ form, of this partial differential equation (PDE), is given by:

$$\mathrm{C}(\psi)\frac{\partial\psi}{\partial t} = \frac{\partial}{\partial z}\left[\mathrm{K}(\psi)\left(\frac{\partial\psi}{\partial z} - 1\right)\right] + \mathrm{S}(z,\psi)\,, \tag{1}$$

where z is the vertical space dimension [L], t is the time dimension [T], $\psi(z,t)$ is the pressure head (suction) [L], $\mathrm{C}(\psi) = d\theta/d\psi$ is the specific moisture capacity [1/L], $\mathrm{K}(\psi)$ is the unsaturated hydraulic conductivity [L/T] and $\mathrm{S}(z,\psi)$ [1/T] is an additional sink term. In our setting[1] [L: cm] and [T: 0.5hrs].

2.1 Initial & Boundary Conditions

To define Equation (1) it is required to provide appropriate initial and boundary conditions:

1. At initial time ($t = 0$), we apply the following initial conditions (IC):

$$\psi(z, t=0) = \psi_0 \in \mathbb{R}^D\,, \tag{2}$$

   where D denotes the dimensionality of the discretized space vector. Since we lack accurate soil moisture (or pressure head) measurements for the vertical spatial domain, which in our case extends to 20m below the surface, we apply an ad–hoc procedure that utilizes the water table depth (i.e. $z_\triangledown$), which is observed at frequent time intervals. Section (4) describes this procedure with more details, along with other numerical and discretization details.

2. At the top of the spatial domain ($z = 0$), we apply a Neumann–type condition by setting the flux equal to the infiltration flux q_{inf}. At the site of our investigation there is no ponding occurring, during rain events, that would introduce a tipping point $t_p > 0$ and change the boundary condition

[1] A summary of the variables with their description is given at the end of the paper in the Notation.

(BC). Moreover, since we neglect other processes such as evapotranspiration, ice melting and surface runoff, this flux is equal to the rainfall (i.e. $q_{\text{inf}} = q_{\text{rain}}$). Therefore we set:

$$\mathrm{K}(\psi)\left(\frac{\partial \psi}{\partial z} - 1\right)\Big|_{z=0} = \min(q_{\text{rain}}(t), 0)\,, \text{ for } t \geq 0\,, \tag{3}$$

where the dependence of the rain flux with time t, is now made explicit.

3. At the bottom of the domain ($z = z_{\text{web}}$), we also apply a Neumann–type condition. Here the assumption is that the water cannot leak downwards to another layer because the saturated hydraulic conductivity of the *fresh bedrock* layer (not included in our model) can be orders of magnitude smaller, comparing to the upper layers, effectively acting as an impermeable bedrock layer [21]. Therefore it is safe to set a zero flux condition:

$$\mathrm{K}(\psi)\left(\frac{\partial \psi}{\partial z} - 1\right)\Big|_{z=z_{\text{web}}} = 0\,, \text{ for } t \geq 0\,, \tag{4}$$

where z_{web} indicates the end of the *weathered bedrock* layer, as highlighted in Figure (1).

2.2 Sink Term

When the model has one spatial dimension (vertical), with zero flux boundary condition at the bottom of the domain, it is imperative to include a mechanism that would allow the water to leave the domain (lateral flow) [31]. Otherwise it is not possible to capture the slow decline of the water table depth, as shown in Figure (2). We do that by introducing the sink term $\mathrm{S}(z, \psi)$, in Equation (1), defined as follows:

$$\mathrm{S}(z, \psi) = \begin{cases} -\alpha_L \psi(z,t), & z \in [z_{\hat{w}}, z_{\triangledown}] \\ 0, & \text{otherwise} \end{cases}\,, \tag{5}$$

where $z_{\hat{w}}$ is the estimated water table depth, $z_{\triangledown}$ is the observed water table and $\alpha_L = 1.5 \times 10^{-3}$ [1/(LT)] is the, hand tuned, lateral conductivity parameter. It is obvious that if $z_{\hat{w}} \geq z_{\triangledown}$ (i.e. the estimated water table is below the observed one), then $\mathrm{S}(z, \psi)$ is zero everywhere. More details on how this term is implemented numerically are given in Section (4).

2.3 Water Retention Curves

The (non–linear) relationship between the soil–water content θ and the pressure head ψ is given by [27, 53]:

$$\theta(\psi) = \theta_{\text{res}} + \frac{\theta_{\text{sat}}(z) - \theta_{\text{res}}}{(1 + (\alpha|\psi|)^n)^m}\,, \tag{6}$$

with $\theta_{\text{res}} \leq \theta(\psi) \leq \theta_{\text{sat}}(z)$. This equation has several (generally unknown) parameters, some of them can be measured directly (θ_{res} and θ_{sat}), while others are fitted parameters (α, m and n). Even though there is a large body of literature that deals with the estimation of these parameters, from experimental data [54, 59, 5, 19, 45], we will not deal with this problem here but rather fix them to some constant values that make reasonable sense in our problem, hence we set $\alpha = 0.0335$ [1/L], $m = 0.5$ and $n = 2$.

The minimum (or residual) water content that stays "trapped" in the underground pores and is unavailable for flow is given by θ_{res}. This parameter can take very small values (not excluding zero in some settings) and in our case is equal to 10^{-3}. On the other hand $\theta_{\text{sat}}(z)$ is the maximum soil moisture content, at a given depth z. We emphasize, that to simplify our framework we assume implicitly that all the porosity is available for water storage (i.e. $\theta_{\text{sat}}(z) \stackrel{\text{def}}{=} \textit{porosity}$). It is common practice to fix this parameter to a constant value; instead in our approach we apply functions that decrease with depth z (i.e. $\theta_{\text{sat}}(z) \to \theta_{\min}$, as $z \to z_{\max}$) .

Figure (3) presents two such examples that are used later in the simulations. The first figure (left panel), shows a "stratified" function where the value of $\theta_{\text{sat}}(z)$ remains constant in the soil layer [0–50 cm], then decreases linearly in the saprolite layer [50–200 cm] and finally drops exponentially to a minimum value $\theta_{\min} > 0$, at the bottom of the domain [2000 cm]. The rationale behind this decision

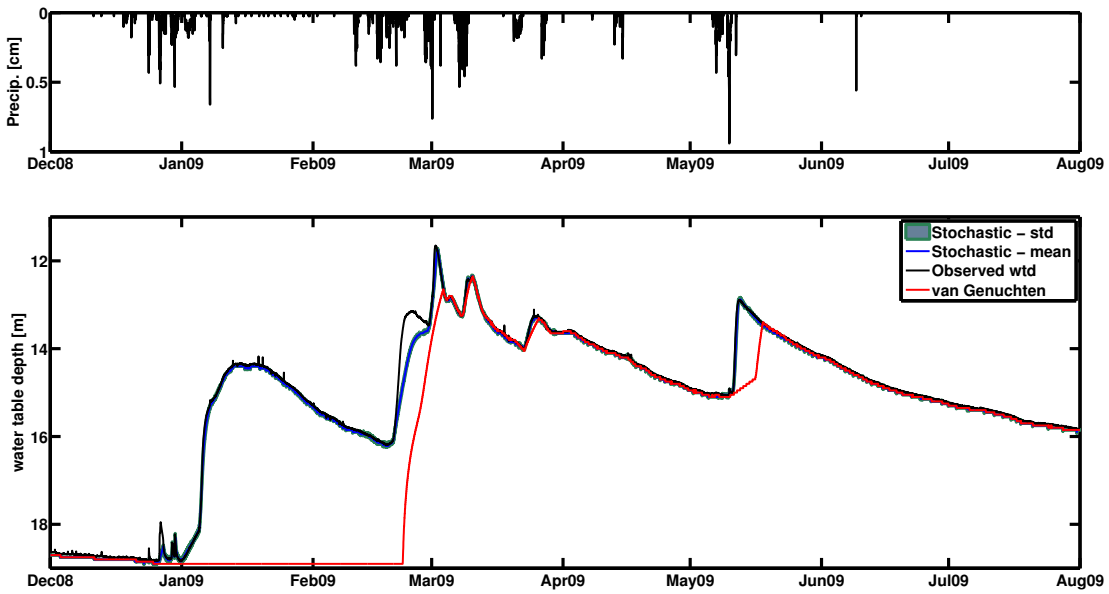

Figure 2: Top panel shows the precipitation data for the WY:08–09. Bottom panel contrasts the results of the current study with mean (blue line) and standard deviation (green shaded area), with the result of the well known, deterministic, van Genuchten (red line), against the observed water table depth values (black line) of "Well–10", for the same dates. Assuming at the surface $z = 0$, the water table values increase towards the bottom of the well. The number of ensembles for this example is set to 50 different realizations.

is that due to inhomogeneities in the underground (especially when modeling medium–large depths), the maximum available water content can vary with depth, i.e. larger values are closer to the surface and smaller values closer to the bottom of the spatial domain. The second figure (right panel), shows an alternative, "noisy", approach where the values of $\theta_{\text{sat}}(z)$ have a decreasing trend as before, but at equidistant predefined depth locations they fluctuate. This could be partially attributed to fractures in the underground that would create more empty (void) space, therefore allowing for more water to be stored in these locations.

Finally, the main parameter of interest in Equation (1) is the hydraulic conductivity $\mathrm{K}(\psi)$, or $\mathrm{K}(\Theta)$ as function of the effective saturation (normalized water content), with

$$\Theta = \frac{\theta(z,t) - \theta_{\text{res}}}{\theta_{\text{sat}}(z) - \theta_{\text{res}}} \ , \ \text{or} \tag{7}$$

$$\Theta(\psi) = \begin{cases} (1 + (\alpha|\psi|)^n)^{-m}, & \psi < 0 \\ 1, & \psi \geq 0 \end{cases} \ , \ \text{with } 0 \leq \Theta \leq 1 \, . \tag{8}$$

Hydraulic conductivity, in the context of hydrogeology, describes the ease with which water can move through pores or fractures. It depends on several properties of the material such as intrinsic (or absolute) permeability, degree of saturation, density and viscosity of the fluid. Accurate estimation of this crucial parameter is a notoriously difficult task, but as it has been observed [4], it is a *scale depended* parameter, i.e. its values can range by several orders of magnitude.

3 Stochastic Hydraulic Conductivity

Traditional (deterministic) approaches for modeling the hydraulic conductivity include the well studied van Genuchten model [53]:

$$\mathrm{K}_{\text{vG}}(\Theta) = \mathrm{K}_{\text{sat}} \sqrt{\Theta} [1 - (1 - \Theta^{1/m})^m]^2 \, , \tag{9}$$

where K_{sat} [L/T], is the maximum value of hydraulic conductivity (at saturation) and Θ, m defined as in Equations (7) and (6), respectively. However, as shown in Figure (2), this model is very slow in

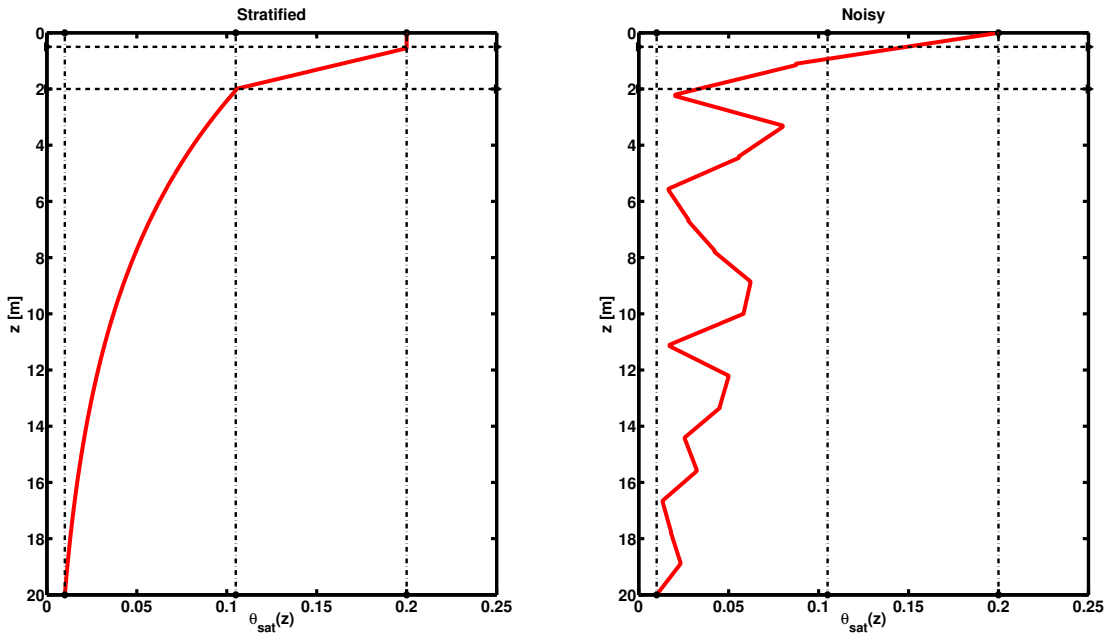

Figure 3: Left panel: stratified porosity profile $\theta_{\rm sat}(z)$, as function of depth z. Horizontal dashed lines indicate the three different soil layers, while the vertical dash–dot lines mark the minimum, medium and maximum porosity values ($\theta_{\rm min}$, $\theta_{\rm med}$ and $\theta_{\rm max}$). Right panel: same as left but for the noisy porosity profile. The locations of "fractures" (i.e. the places where porosity changes rapidly), were set at equidistant locations and the porosity values were chosen at random.

capturing the fast response of the water table to the first rains, with dry initial conditions, as those found in California.

Natural heterogeneity of underground aquifer materials, along with complex spatial structures suggests that most of the realistic problems in hydrogeology should be treated in a probabilistic manner [16]. The importance of stochastic modeling in hydrogeology is highlighted in [58, 43, 15], however as [38] argues, the use of stochastic methods in real world applications is still in its infancy. A general introduction into the subject is given by [42].

Therefore, following the shortcomings of well known deterministic approaches in capturing the water table dynamics, this work proposes a *stochastic* model for the hydraulic conductivity, as follows:

$$\mathrm{K_{stc}}(\Theta) = \Theta^{\lambda}\mathrm{K_{bkg}}\ , \text{with } \mathrm{K_{bkg}} \sim \mathrm{LogN}(\nu, \Lambda)\ , \tag{10}$$

where $\Theta \in [0,1]$ is the effective saturation, $\lambda > 0$ is a tuning parameter and the Log–Normal probability density function (pdf), is given by:

$$f_{\mathrm{K_{bkg}}}(\kappa;\nu,\Lambda) = \frac{1}{\kappa\sqrt{2\pi}\Lambda}\exp\left\{-\frac{(\ln\kappa-\nu)^2}{2\Lambda^2}\right\}\ . \tag{11}$$

We use the stochastic part of the equation (i.e. $\mathrm{K_{bkg}}$), to mimic the effect of the naturally occurring heterogeneity in the underground, as well as the fractures that would allow the water to move faster by providing preferential paths with higher conductivity. The approach presented here is simple and very flexible. $\mathrm{K_{bkg}}$ is defined such as (see also Appendix A):

$$\langle \mathrm{K_{bkg}} \rangle = \mu(z)\ , \tag{12}$$

$$\mathrm{Var}[\mathrm{K_{bkg}}] = \Sigma(1-\Theta)\ , \tag{13}$$

where the angle brackets $\langle\cdot\rangle$ denote expected value, the noise amplitude $\Sigma \in \mathbb{R}^+$ and $\mu(z) \geq 0, \forall\ z \in [0, z_{\rm web}]$, defined piecewise by:

$$\mu(z) = \begin{cases} \mathrm{K_{sat}^{soil}}, & 0 \leq z \leq z_{\rm soil} \\ -a_l z + b_l, & z_{\rm soil} < z \leq z_{\rm sap} \\ a_e \exp\{-z b_e\}, & z_{\rm sap} < z \leq z_{\rm web} \end{cases}\ . \tag{14}$$

The scale and offset parameters of Equation (14) are set to:

$$a_l = -\frac{\mathrm{K}_{\mathrm{sat}}^{\mathrm{sap}} - \mathrm{K}_{\mathrm{sat}}^{\mathrm{soil}}}{L_{\mathrm{sap}}}, \quad b_l = -\frac{\mathrm{K}_{\mathrm{sat}}^{\mathrm{sap}} z_{\mathrm{soil}} - \mathrm{K}_{\mathrm{sat}}^{\mathrm{soil}} z_{\mathrm{sap}}}{L_{\mathrm{sap}}},$$
$$a_e = \mathrm{K}_{\mathrm{sat}}^{\mathrm{sap}} \left(\frac{\mathrm{K}_{\mathrm{sat}}^{\mathrm{sap}}}{\mathrm{K}_{\mathrm{sat}}^{\mathrm{frs}}} \right)^{\frac{z_{\mathrm{sap}}}{L_{\mathrm{web}}}}, \quad b_e = \ln \left(\frac{\mathrm{K}_{\mathrm{sat}}^{\mathrm{sap}}}{\mathrm{K}_{\mathrm{sat}}^{\mathrm{frs}}} \right) L_{\mathrm{web}}^{-1},$$

with $\mathrm{K}_{\mathrm{sat}}^{\mathrm{soil}}$, $\mathrm{K}_{\mathrm{sat}}^{\mathrm{sap}}$ and $\mathrm{K}_{\mathrm{sat}}^{\mathrm{frs}}$, defining the saturated hydraulic conductivity values at the top of the soil, saprolite and fresh bedrock respectively, $L_{\mathrm{sap}} = z_{\mathrm{sap}} - z_{\mathrm{soil}} > 0$ and $L_{\mathrm{web}} = z_{\mathrm{web}} - z_{\mathrm{sap}} > 0$, such that the mean function $\mu(z)$ is continuous over the whole spatial domain.

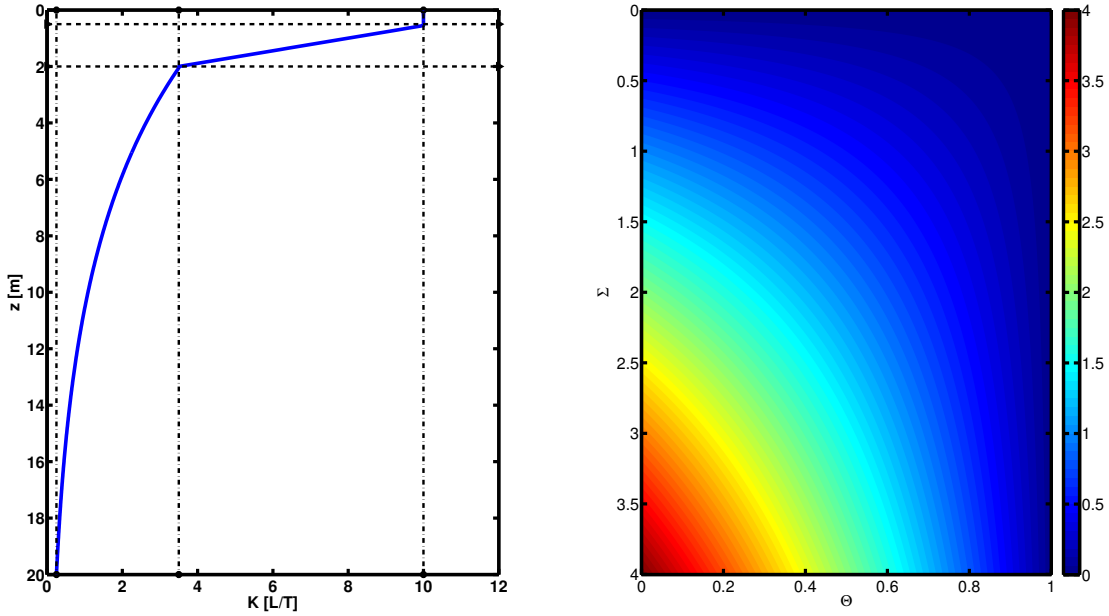

Figure 4: Left panel: mean function $\mu(z)$, as function of depth z. Horizontal dashed lines separate the three different soil layers, while the vertical dash-dot lines mark the corresponding saturated hydraulic conductivity values ($\mathrm{K}_{\mathrm{sat}}^{\mathrm{frs}}$, $\mathrm{K}_{\mathrm{sat}}^{\mathrm{sap}}$ and $\mathrm{K}_{\mathrm{sat}}^{\mathrm{soil}}$), for each layer. Right panel: profile of $\mathrm{Var}[\mathrm{K}_{\mathrm{bkg}}]$, as function of noise amplitude Σ and effective saturation Θ. The value of λ is fixed to 1.

Figure (4), presents two characteristic examples of these equations. The left hand side figure shows how the mean function $\mu(z)$ (blue line), remains constant in the soil layer, then declines linearly in the saprolite layer and finally drops exponentially on the weathered bedrock layer. The choice of $\mathrm{K}_{\mathrm{sat}}^{\mathrm{soil}}$, $\mathrm{K}_{\mathrm{sat}}^{\mathrm{sap}}$ and $\mathrm{K}_{\mathrm{sat}}^{\mathrm{frs}}$ can be found by direct measurements in the predefined locations, or estimated by other techniques. In the right hand side figure, since it is depth independent, is obvious that the variance maximizes in the absence of water Θ and for high values of noise amplitude Σ. We emphasize that the mean function can be modified to match specific *site–characteristics*, thus making the approach more broadly available.

The idea of saturation-dependent variance is better illustrated in Figures (5), (6), and (7). In the absence of water ($\Theta = 0$), there are various possible paths that the new incoming water can "choose" to pass through, Fig. (5). Some of them might be more conductive (green lines) than others (red lines). Therefore, the uncertainty on which path will be chosen is maximum. When the soil becomes partially saturated Fig. (6), that will have an effect of the preferable paths (some paths with increased saturation might attract more water than others with less saturation).

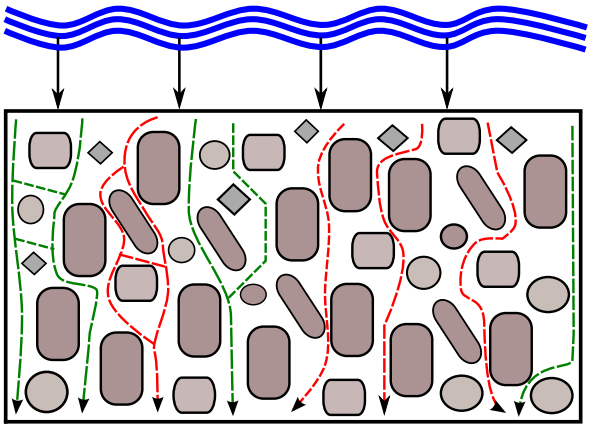

Figure 5: Schematic illustration of a soil grid cell. Different shapes represent different types of gravel. Green lines indicate paths of (potentially) higher conductivity, while red paths indicate less conductive paths. The absence of water in the soil increases the variance of K_{bkg} to its maximum value (i.e. many probable paths for the incoming water – blue wave lines).

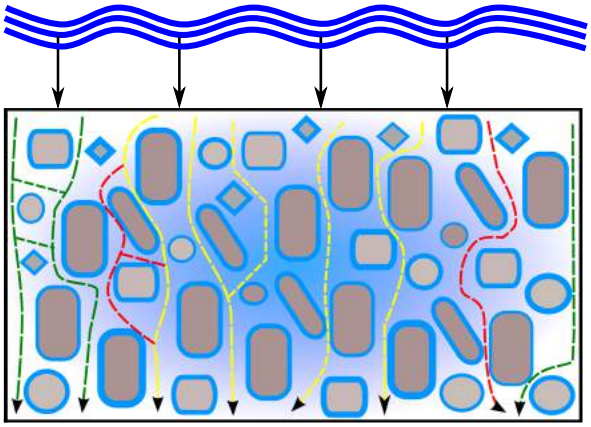

Figure 6: Same as Figure (5), but for partially saturated soil. The presence of water, attached on the gravels (blue color) alters the probability of paths for the water (yellow dashed lines).

Finally, in the case of complete saturation Fig. (7), the water is assumed to be moving as a continuous medium, therefore the variability on the chosen paths does not change in time (i.e. $Var[K_{bkg}] = 0$).

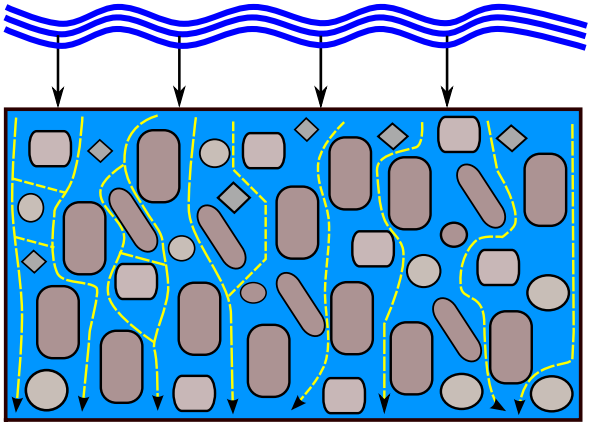

Figure 7: Same as Figure (5), but for fully saturated soil. In this case the water is depicted as a continuous medium, therefore there is no variability on paths with higher or lower hydraulic conductivity (i.e $Var[K_{bkg}] = 0$ and $Var[K_{stc}(\Theta)] = 0$).

It follows that hydraulic conductivity $\mathrm{K}_{\mathrm{stc}}(\Theta)$, will also have a Log–Normal distribution with mean and variance functions given by:

$$\langle \mathrm{K}_{\mathrm{stc}}(\Theta) \rangle = \Theta^{\lambda} \mu(z) \,, \tag{15}$$

$$\mathrm{Var}[\mathrm{K}_{\mathrm{stc}}(\Theta)] = \Theta^{2\lambda} \Sigma (1 - \Theta) \,. \tag{16}$$

Note, that since the random variable $\mathrm{K}_{\mathrm{bkg}}$ is defined such that its variance vanishes at full saturation ($\Theta = 1$), it implies that the saturated hydraulic conductivity $\mathrm{K}_{\mathrm{sat}} \equiv \mu(z)$, becomes a function of depth z.

Figure (8) shows the mean Eq. (15), as profile of depth z and effective saturation Θ and variance Eq. (16), as profile of Σ and Θ respectively, for fixed $\lambda = 1$. It is evident that the soil and saprolite layers have higher conductivity values, therefore allowing the water to penetrate faster into the deeper underground layers.

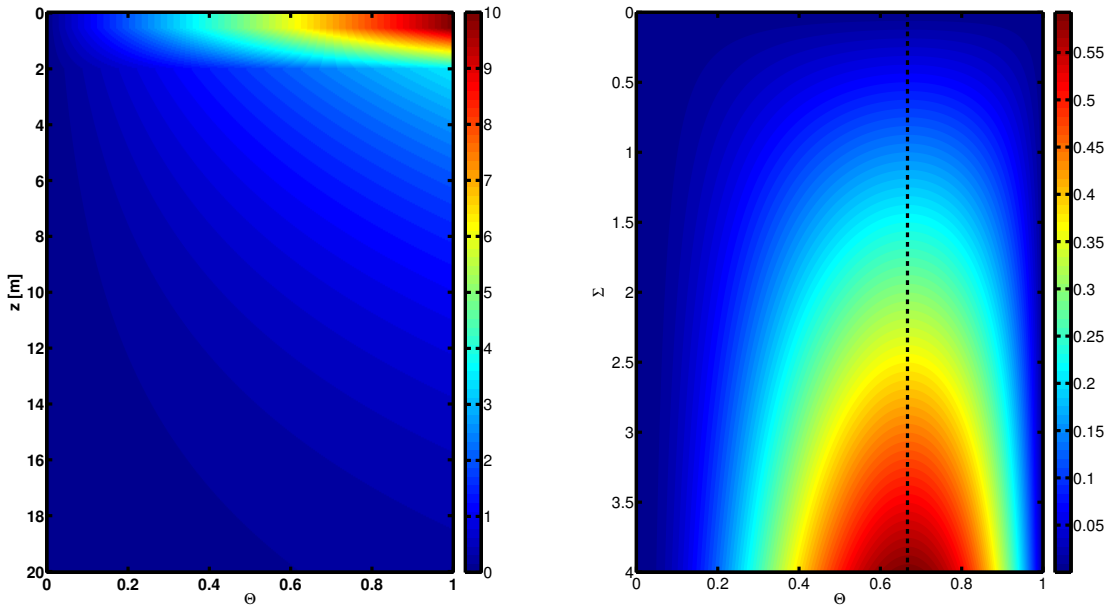

Figure 8: Left panel: profile of the mean hydraulic conductivity $\langle \mathrm{K}_{\mathrm{stc}}(\Theta) \rangle$, as function of depth z, for a fixed parameter values ($\Sigma = 2$, $\lambda = 1$). Note that because $\mathrm{K}_{\mathrm{bkg}}$ decreases with depth z, the hydraulic conductivity also inherits this property. Right panel: profile of the hydraulic conductivity variance $\mathrm{Var}[\mathrm{K}_{\mathrm{stc}}(\Theta)]$, as function of noise amplitude Σ and effective saturation Θ, for a fixed value of $\lambda = 1$. The vertical dashed line indicates the saturation level at which the variance maximizes, independently of the Σ value.

The choice of a Log–Normally distributed hydraulic conductivity is not new, as shown in [14, 9, 8, 13] and references therein. This is also supported by experimental data in several studies including [22, 56, 3].

A typical example of the proposed stochastic $\mathrm{K}_{\mathrm{stc}}(\Theta)$, along with the corresponding $\mathrm{K}_{\mathrm{bkg}}$, are shown in Figures (9) (left panel) and (10). These plots are generated from a single noise realization and it is apparent that due to the noisy nature of $\mathrm{K}_{\mathrm{bkg}}$, there are high conductivity values at deep locations in the underground that would allow the water to move faster. We contrast this with the right panel of Figure (9), where the van Genuchten model is used for the same depth z and saturation values Θ. Note that for this model to produce high conductivity values requires highly saturated soils ($> 60\%$), which translates to holding the water at the same locations (underground cells) for longer periods of time causing saturation at depths near the surface.

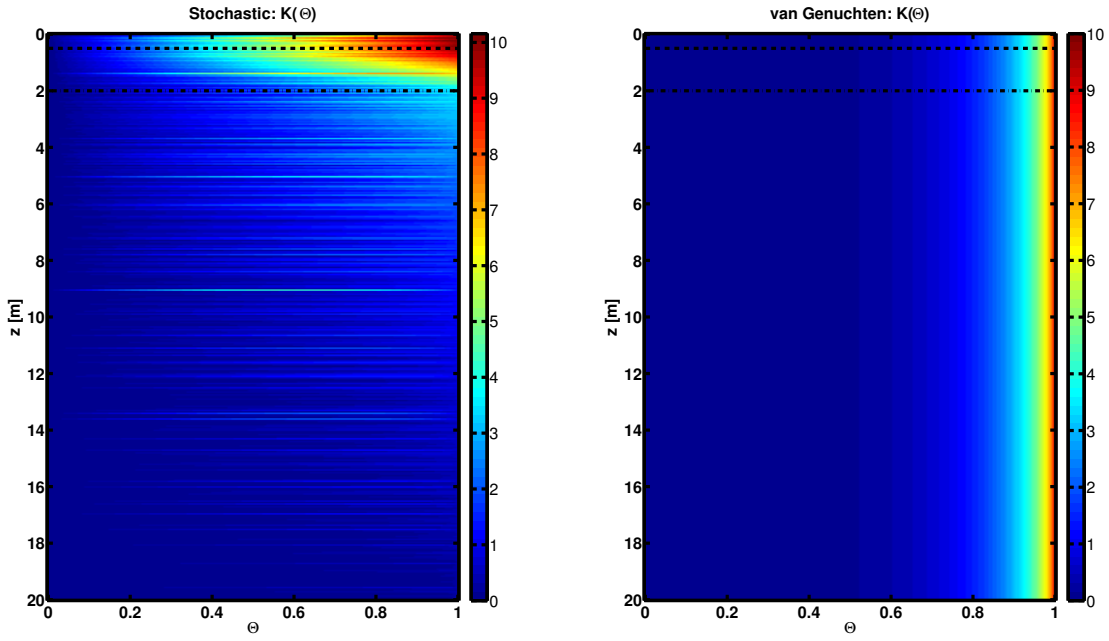

Figure 9: Comparison of the $K_{stc}(\Theta)$ (left panel), from a single noise realization with $\Sigma = 2$ and $\lambda = 1$, with the $K_{vG}(\Theta)$ (right panel), with $K_{sat} = 10$ and $m = 0.5$. Both plots are presented as functions of depth z and normalized soil moisture Θ. Dashed lines mark the end of soil and saprolite layers. The units are [L/T].

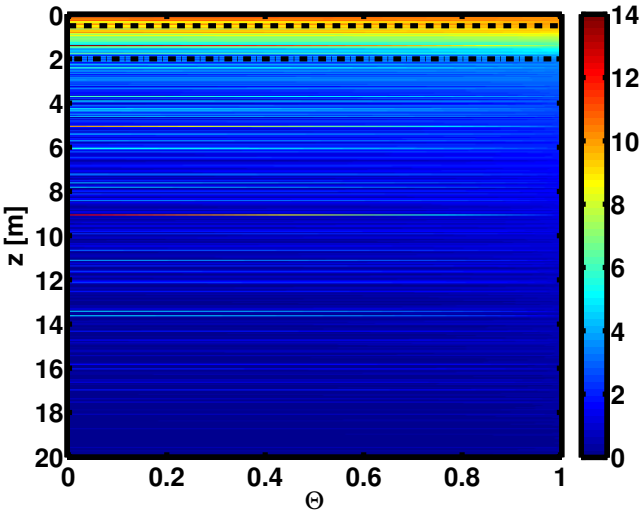

Figure 10: Profile, for a single noise realization with noise amplitude $\Sigma = 2$, of the K_{bkg}, as function of depth z and normalized soil moisture Θ. Dashed line marks the end of soil layer, whereas dashed-dotted line indicates the end of saprolite layer. The units are [L/T].

To make the comparison more clear visually, we present the difference of the two examples in Figure (11). Note that (i) the yellow color highlights positive values (i.e. where the new model is higher than the van Genuchten) and only for $\Theta = 0$ the two results match exactly, and (ii) the noise does not reduce directly with the depth z, but rather with the degree of effective saturation, i.e. as $\Theta \to 1$ the wiggles decrease.

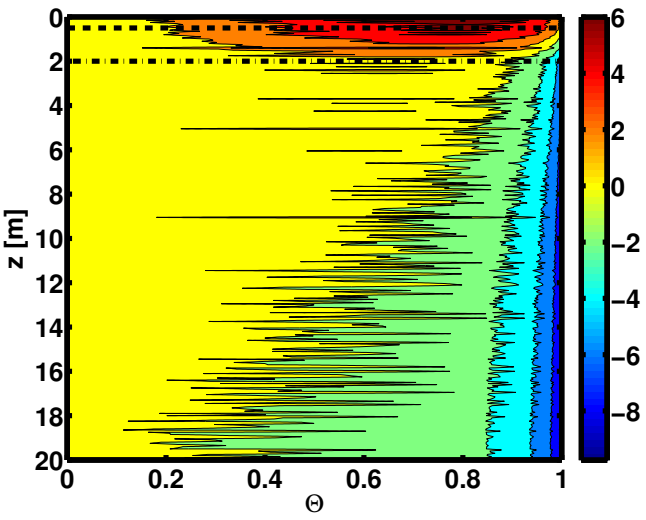

Figure 11: Difference of the hydraulic conductivities ΔK, between the new stochastic approach and the van Genucthen as shown in Figure (9). Note that the noise on ΔK does not vary with depth z, but with the degree of saturation Θ. Therefore at each depth higher saturation values ($\Theta \to 1$), lead to noise reduction.

The last note on the noise can be further illustrated with Figure (12). These plots show an example of K_{bkg} with the same noise realization, but for different degrees of saturation $\Theta = [0, 0.25, 0.75, 1]$. It is apparent that the noise is invariant of the depth, but decreases to zero at full saturation.

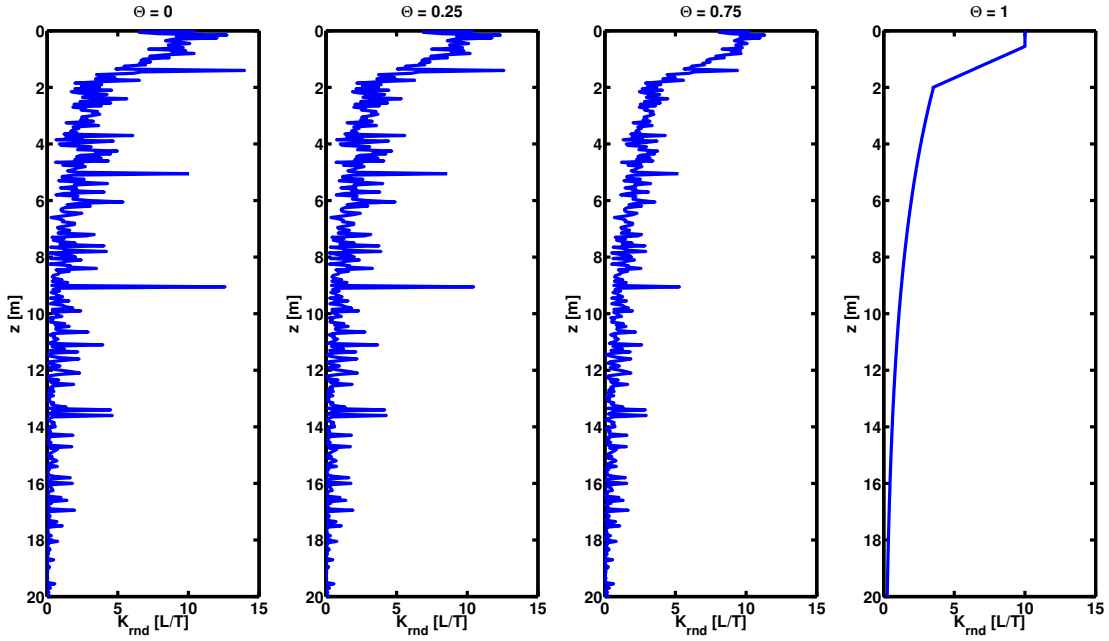

Figure 12: A typical example of the stochastic variable K_{bkg}, as function of depth z with different values of effective saturation Θ. From left to right the degree of saturation increases from 0% (completely dry), to 100% (full saturation). The saturation is assumed uniform in the whole spatial domain.

4 Numerical Solution

Before proceeding to the experimental part of our work, along with the description of our results, we provide a detailed presentation of our numerical treatment to the problem to make our approach more clear. Our problem setup involves the numerical solution of Richards' equation, with an additional sink term as shown in Equation (1), for variably saturated soils.

4.1 Numerical Method

Richards' equation is a highly non-linear PDE (parabolic in the unsaturated zone and elliptic in the saturated zone), thus exact closed–form solutions exist only is some special cases. The usual approach is to discretize the equation, in space and time, and solve it numerically. There is a plethora of methods for the solution of this PDE that can be largely categorized into (a) finite difference [18, 20, 37, 35, 6, 40, 7], (b) finite element [62, 29, 26, 34], (c) finite volume [11, 36] and (d) other hybrid approaches [2, 41, 60].

We will not pursue this discussion here but rather mention briefly the method of choice that used to solve our problem. Our numerical approach is based on the so called *method of lines* (MOL) [46]. This is a very popular approach for variable step size, variable-order temporal integration [47] and has also attracted attention in hydrology [52, 25, 57, 24]. The MOL decouples the temporal and spatial approximations of a given solution to a system of differential algebraic equations (DAE). The motivation behind this approach is that the temporal integration aspects of the problem can be handled optimally by state of the art algorithms designed to solve systems of stiff ordinary differential equations (SODE), or differential algebraic equations (DAE).

Here we apply a modified version of MATLAB$^{\text{TM}}$ function `pdepe` (tailored and optimized to our specific PDE), which is based on second order discretization in space [51] and variable order (adaptive) in time.

4.2 Spatial Discretization

We begin by first splitting the vertical spatial domain in three main (virtual) underground layers. These are (i) the *soil* layer, with depth 0.5m, (ii) the *saprolite* layer, with depth 1.5m and (iii) the *weathered bedrock* layer, which for our case study "Well–10", extends to 18.5m. Figure (1), presents an abstract illustration with depth values z increasing downwards ($z = 0$ at the surface). The labels z_{soil}, z_{sap} and z_{web} indicate the end of each of the three layers. We choose to discretize our domain uniformly in centimeter units [cm] and set these three labels at 50, 150 and 2000 [cm] respectively.

We tried various discretizations steps Δz. Table (1), shows the impact of different step sizes, ranging from 1cm up to 10cm, measured on two different statistics (see Section 5.1). The forth column (CPU), shows the execution time for each simulation. As expected if we try a very fine space step (e.g. Δz = 1cm) the results are optimal, in terms of measured errors, however the computational cost would be prohibitively high for our simulations. Moreover, the memory demands also increase with finer resolution, as shown in columns five (D) and six (MEM). Therefore, we concluded that a step size of Δz = 5cm would suffice, by providing numerically accurate results in reasonable computational time.

Δz [cm]	RMSE [cm]	NSC [%]	CPU [sec]	D	MEM [bytes]
1	11.9	99.5	1.701×10^4	2001	1.6×10^4
2	12.3	99.4	1.075×10^4	1001	8.0×10^3
4	13.2	99.3	6.742×10^3	500	4.0×10^3
5	14.0	99.3	5.974×10^3	401	3.2×10^3
8	16.7	98.7	4.057×10^3	250	2.0×10^3
10	18.5	98.7	3.720×10^3	201	1.6×10^3

Table 1: Effect of space discretization Δz, on the numerical solution of Richards' PDE. The table summarizes results for the Root Mean Square Error (RMSE), the Nash-Sutcliffe Coefficient (NSC) as percentage %, the CPU time in seconds, the dimensionality of the state vector D and the allocated memory MEM (per single state vector) in bytes. All six simulations used the same parameter setting and identical initial conditions. The yellow colored row (at Δz = 5) indicates the space resolution of our choice.

4.3 Estimation of Saturated Zone

For many types of soils there is an *effective air–entry* tension ψ_{sat} [18]. This value acts like a "threshold" in our approach and any cell with $\psi(z) \geq \psi_{\text{sat}}$, is considered fully saturated $\theta(z) = \theta_{\text{sat}}(z)$ (i.e. $\Theta = 1$). Ideally, this value is found when the specific moisture capacity becomes zero, $C(\psi) = 0$, in Equation (1).

Given the fact that we have chosen Equation (6), as the water retention curve, the specific moisture capacity is given by:

$$\mathrm{C}(\psi) = -\mathrm{sgn}(\psi)\,\alpha^n\, m\, n\, (\theta_{\mathrm{sat}} - \theta_{\mathrm{res}})\,\Theta^{\frac{m+1}{m}}\,|\psi|^{n-1}\,, \tag{17}$$

which becomes equal to zero at $\psi = \psi_{\mathrm{sat}} = 0$.

Even though $\frac{\partial\theta}{\partial t}$ and $(\frac{d\theta}{d\psi}\frac{\partial\psi}{\partial t})$ are mathematically equivalent in continuous space, their discretized analogs are not. This discrepancy, in the discrete form, is attributed due to the highly non–linear nature of the specific moisture capacity term $\mathrm{C}(\psi) \equiv \frac{d\theta}{d\psi}$. This leads to significant mass balance errors in the ψ-based formulations. To improve the numerical stability of our algorithm instead of allowing $\mathrm{C}(\psi) = 0$, at saturation, we set it to a very small positive value $\epsilon = 10^{-6}$. Next, solving Equation (17) for ψ_{sat} (i.e. $\mathrm{C}(\psi_{\mathrm{sat}}) = \epsilon$), we get $\psi_{\mathrm{sat}} = -1.8 \times 10^{-3}$ cm, assuming that the rest of the parameters, such as m, n, α, etc., are known. Therefore, any cell with pressure head value $\psi(z) \geq -1.8 \times 10^{-3}$ cm, is assumed to be fully saturated.

4.4 Runoff Approximation

The high frequency data available from the `Rivendell` site reveal a rapid rise of the water table after first rains of the season, followed by a relatively slow recession, presumably as a result of flow down the hill-slope. This is shown in Figure (2), where the observed water table ($z_{\triangledown}$) is shown with the black solid line. In order to capture the dynamics of the water table in the one-dimensional model, we include a sink term $\mathrm{S}(\psi)$, as defined by Equation (5) to mimic lateral flow that removes water from the water table.

This is achieved by "guiding" the PDE solver to produce a solution that would match the estimated water table $z_{\hat{w}}$, with the observed one $z_{\triangledown}$, in thirty minutes time intervals. We emphasize that the sink term is not applied once at the end of the thirty minutes time window; removing in one stroke the 30-minute accumulation of excess water in the over saturated cells would introduce serious imbalances to the solution of the PDE and violate the actual physics of the problem. Instead, the water table information is used adaptively, at each intermediate time step of the PDE solver (e.g. for every $\delta\tau = 5$ sec), by subtracting a very small amount of water only when the currently estimated $z_{\hat{w}}$ exceeds the $z_{\triangledown}$. On the other hand, if the estimated solution produces a $z_{\hat{w}}$ which is below that observed, the sink term is set to zero.

Figure (13) illustrates the approach we employ for estimating the "runoff". This approach is based on solving the PDE twice between two time instants (e.g. t_{k-1} and t_k, with $\Delta t_k = t_k - t_{k-1} = 30$ min). The first pass from $\psi(t_{k-1})$ to $\psi(t_k)$ (blue letters), produces a solution with the sink term $\mathrm{S}(\psi)$, while the second pass $\psi_{\setminus s}(t_k)$ (red letters), does not include the sink term. Subsequently, both pressure head vectors are converted to volumetric water content and then they are subtracted, $\Delta\theta(z, t_k) = \theta_{\setminus s}(t_k) - \theta(t_k)$. The produced vector contains the additional water that the domain would have if the sink term was not in place.

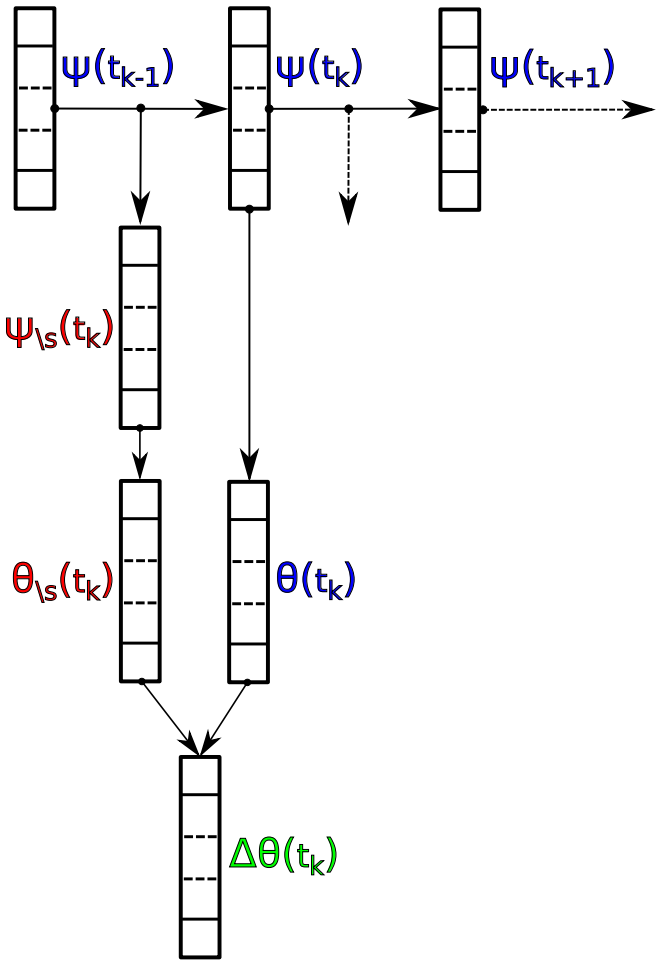

Figure 13: Schematic illustration of the numerical approximation of the runoff. The discrete vector representations with blue label on their right side are computed with the sink term (e.g. $\psi(t_k)$, $\theta(t_k)$), whereas the vectors with the red labels on their left side are computed without the sink term (e.g. $\psi_{\setminus s}(t_k)$, $\theta_{\setminus s}(t_k)$). The runoff $\mathrm{R}(t_k)$ is computed by integrating $\Delta\theta(t_k)$ on the vertical domain.

Finally to compute the "runoff" R(t) at time t_k, we integrate (numerically) the vector over the spatial domain z:

$$\mathrm{R}(t_k) = \Delta z \sum_{j=1}^{D} \Delta\theta(z_j, t_k)\,, \tag{18}$$

assuming a uniform Δz. Even though this procedure requires twice the amount of time to solve the PDE, it provides a very simple and straightforward way to approximate the excessive water that has departed from the domain.

4.5 Initial Conditions: ψ_0

This section concludes with a brief note on the initialization of the vector ψ_0 (initial conditions). Since it is easier to conceptualize in terms of water content (rather than pressure head), the process is described in term of $\theta(z,t)$ values. In the absence of measurements that would give us an accurate (or even partial) knowledge of the water conditions in the underground we start by specifying a "first–guess" state vector, arbitrarily chosen to have water content proportional to the porosity, ranging from 10% around the surface up to 100% near the bottom of the well.

Since the location of the water table $z_\triangledown$ is known a priori, any discrete cell below that depth is fully saturated $\theta(z \geq z_\triangledown, t_0) = \theta_{\mathrm{sat}}(z \geq z_\triangledown)$. Solving Equation (6) for ψ, we transform the water content values to the corresponding pressure head values. Since our integrations start at the end of the dry season, we assume no additional forcing (such as precipitation) acting on the PDE and using zero flux boundary conditions. From the "first–guess" profile, we spin–up RE until the solution reaches a steady

state. During this process we use the sink term S(ψ) to remove any excess water. Thus, after a small number of iterations we obtain a state vector which is saturated below the observed water table and stable states above.

This method produces an initial condition vector $\psi_0(z)$ that is used later for the simulations. Depending on the hydraulic conductivity model K(Θ), this vector can vary in water content. The stochastic model we propose here produces rather dry initial conditions (above the water table), while other models, such as the van Genuchten gives rise to much wetter conditions for the same specified water table. However, we argue that our approach is more suitable for the site we examine here, since precipitation in California is very limited, which would justify fairly dry soils for initial conditions.

5 Experimental Setup & Results

The current study presents an analysis of this new stochastic approach focusing on the data from "Well–10", whose surface is about 60 meters higher than the Elder Creek on a steep ($\sim$ 35 degrees) hill–slope. We analyze data between the dates `01-Dec-2008` and `31-Jul-2009` (henceforth WY:08–09), a period with continuous data for precipitation [cm] and water table [m], at $\Delta t = 30$ minute time intervals, without missing values or instrumental issues that required re-calibration. Table (2) summarizes the parameter setting in several groups, such as spatial, temporal, etc., to make their presentation easier and unless stated otherwise they were kept fixed for all the simulations in this section.

Group	Variable	Value	Units
Spatial	z_0	0	[cm]
	z_{soil}	50	[cm]
	z_{sap}	200	[cm]
	z_{web}	2000	[cm]
	Δz	5	[cm]
Temporal	t_0	0	[hr]
	t_F	8640	[hr]
	Δt	0.5	[hr]
Soil Moisture	θ_{res}	0.001	[cm^3/cm^3]
	θ_{min}	0.01	[cm^3/cm^3]
	θ_{max}	0.2	[cm^3/cm^3]
	α	0.0335	[1/cm]
	n	2	[-]
	m	0.5	[-]
Stochastic Model	$\text{K}_{\text{sat}}^{\text{soil}}$	20	[cm/hr]
	$\text{K}_{\text{sat}}^{\text{sap}}$	7	[cm/hr]
	$\text{K}_{\text{sat}}^{\text{frs}}$	0.5	[cm/hr]
	Σ	2	[-]
	λ	1	[-]
Other	ϵ	10^{-6}	[1/cm]
	ψ_{sat}	-0.0018	[cm]

Table 2: Summary of the parameter setting for the experiments. The parameters are grouped in spatial, temporal, soil moisture, stochastic model and other.

5.1 Estimation of Σ and λ

In order to estimate the optimal values for the noise amplitude Σ and the exponent λ, we introduce two measures to compare the performance of the algorithm on different parameter settings. To assess the model bias, we use the root mean-square error (RMSE) and the Nash–Sutcliffe coefficient (NSC)

[28].

$$\text{RMSE} = \sqrt{\frac{1}{N}\sum_{k=1}^{N}\left(z_{\hat{w}}^{(k)} - z_{\triangledown}^{(k)}\right)^2}, \tag{19}$$

$$\text{NSC} = 1 - \frac{\sum_{k=1}^{N}\left(z_{\hat{w}}^{(k)} - z_{\triangledown}^{(k)}\right)^2}{\sum_{k=1}^{N}\left(\bar{z}_{\triangledown} - z_{\triangledown}^{(k)}\right)^2}, \tag{20}$$

with N denoting the total number of discrete time points and $z_{\hat{w}}^{(k)}$, $z_{\triangledown}^{(k)}$ the estimated and observed depths of the water table respectively, where index k is shorthand notation for $t_k = t_0 + k\Delta t$ and $\bar{z}_{\triangledown} = \frac{1}{N}\sum_{k=1}^{N} z_{\triangledown}^{(k)}$.

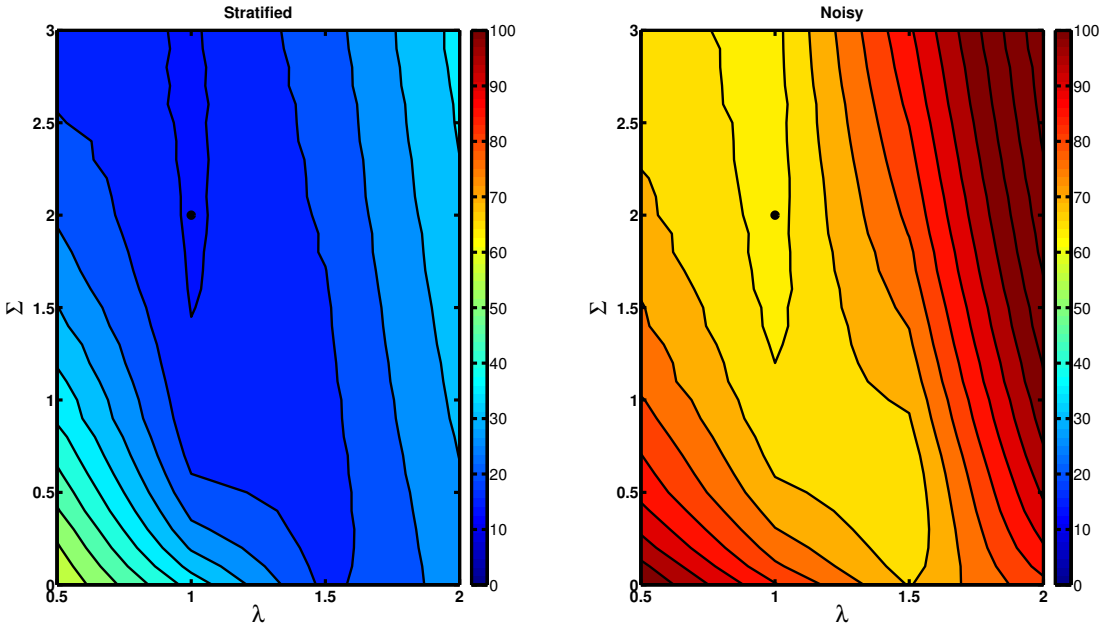

Figure 14: Root mean square error (RMSE), as function of noise amplitude Σ and exponent λ. The black circle indicates the setting with the best performance (Σ = 2, λ = 1). Left panel shows the results with the stratified porosity profile, whilst the right panel with the noisy profile.

The NSC measure is equivalent to the coefficient of determination R^2 (used in statistics literature) and is commonly applied in hydrological modeling to assess accuracy of predictive performance. It compares the performance of the model (mean forecast), with the performance of the climatological forecast $\bar{z}_{\triangledown}$. The values can also be converted to percentages, so that 100% indicates optimal match between the observed and the forecasted values. Unlike RSME where low values indicate less bias, NSC scores greater than 0% indicate higher performance to the climatological mean.

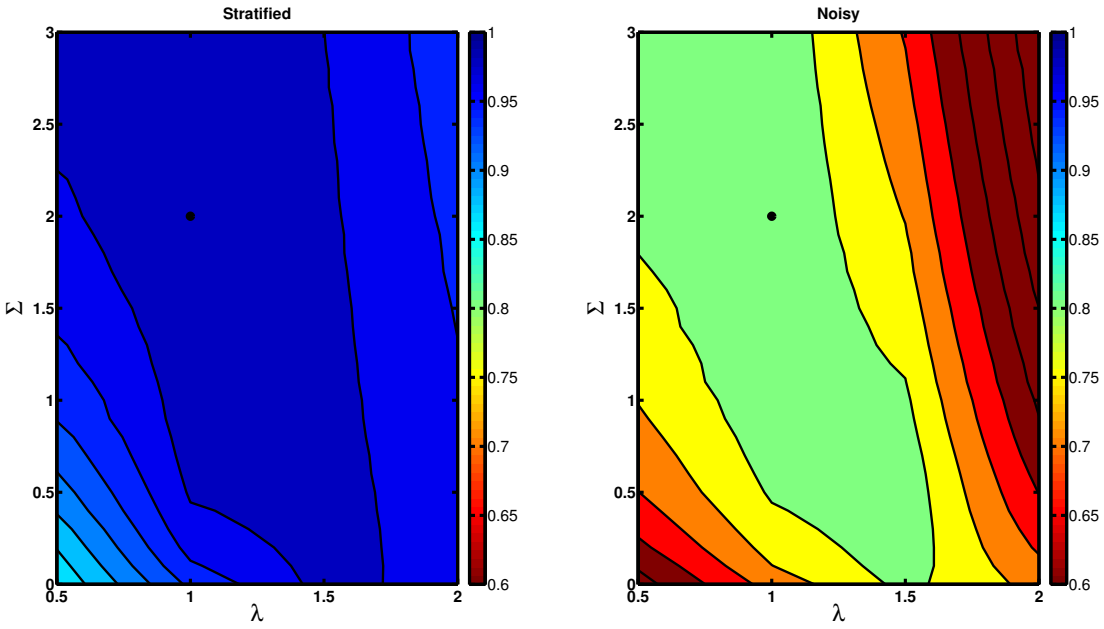

Figure 15: Nash-Sutcliffe coefficient (NSC) as function of noise amplitude Σ and exponent λ. The black circle indicates the setting with the best performance ($\Sigma = 2$, $\lambda = 1$). Left panel shows the results with the stratified porosity profile, whilst the right panel with the noisy profile.

Figure (14) presents the RMSE results of two extensive simulations, one with the stratified (left panel) and one with the noisy porosity profile respectively (right panel), for a range of different $\Sigma \in \{0, \ldots, 3\}$ and $\lambda \in \{0.5, \ldots, 2\}$ values. The initial conditions ψ_0, for all trials were identical and the rest of the parameters were kept fixed to predefined values.

Even though different ranges of RSME result for the two porosity profiles, the same combination of λ - Σ produces optimal results with best parameter setting at $\Sigma = 2$ and $\lambda = 1$. Similarly, Figure (15) shows the results for the NSC. Despite the fact the λ - Σ regions of high NSC are quite large, they point at the same parameter setting for optimal results as the RMSE plots.

5.2 Monte Carlo Results

After identifying the parameter values for Σ and λ which provide optimal results, in terms of the predefined statistics (Eq. 19 and 20), we performed fifty Monte Carlo simulations, with different noise realizations of the K_{bkg} and evaluated the average behavior of this new stochastic model against the widely-used deterministic van Genuchten hydraulic conductivity model, with the two predefined porosity profiles.

The results are presented below for the two porosity profiles, $\theta_{sat}(z)$, whose values range from $\theta_{max} = 0.2$ [cm^3/cm^3] at the top of the surface layer, to $\theta_{min} = 0.01$ [cm^3/cm^3] at the bottom of the weathered bedrock layer, as shown in Figure (3).

5.2.1 Water content and related quantities

The ensemble mean of the volumetric water content $\theta(z, t)$, from fifty different noise realizations of the new stochastic model, is shown in Figure 16(a), for the *stratified* porosity profile (left panel). The right panel shows the results of the van Genuchten model, for the same time period, with the same porosity profile. The results are plotted as function of depth z [m] and time t (in months) for the WY:08–09, on logarithmic scale ($\log_{10}$), with the actual observations of the water table z_∇ superimposed (shown with the black dashed line).

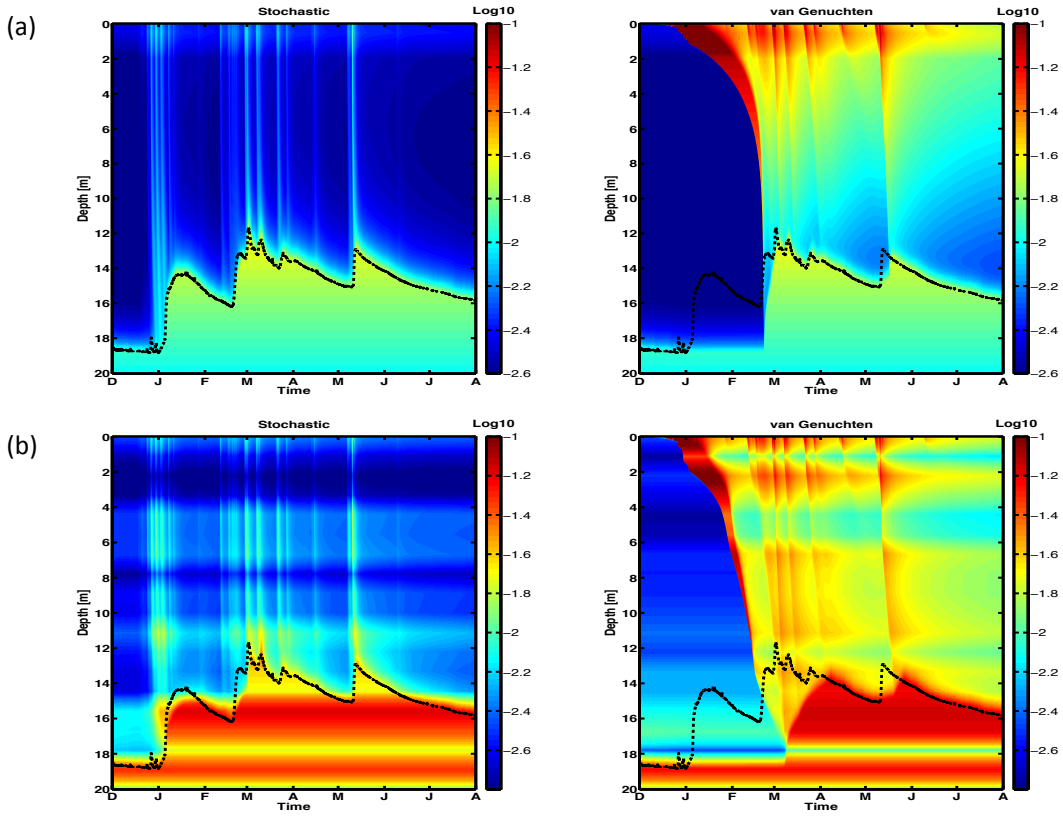

Figure 16: Volumetric water content $\theta(z,t)$ [cm^3/cm^3] results, with (a) the stratified and (b) the noisy porosity profiles respectively. Left panel shows the ensemble mean of the new model, on the logarithmic scale ($\log_{10}$), from 50 noise realizations. The setting for this example is $\Sigma = 2$, $\lambda = 1$. The right panel shows the corresponding results with the van Genuchten model (one model run). In both plots, the vertical dimension represents the depth z [m] and the horizontal is time (in months). The black dashed line shows the observed water table depth for the whole WY:08–09.

With the stochastic hydraulic conductivity model results, the bright light-blue paths that run from the surface to the water table show the rapid water movement after the rain events, while dark blue colors indicate drier soils. With the van Genuchten hydraulic conductivity, the water does not penetrate to depth until the upper soil mantle has a high water content (areas with red color). It is evident that in this example the new approach captures the fast responses of the water table to the first winter rain events with great accuracy.

Similarly, Figures 16(b) and 17(b) show the outcomes of the volumetric water content and the effective saturation, respectively, but with the *noisy* porosity profile. Again, the left panels illustrate the average results from fifty simulations of the stochastic model, with different noise realizations, compared to the one obtained with the van Genuchten model, from a single model run (right panel). Despite the fact that the estimation of the saturated zone is good for most of the time period, we find it slightly inferior to the one presented earlier with the *stratified* porosity profile, by missing the actual water table by a few meters, especially during the months of Jan-2009 and Mar-2009.

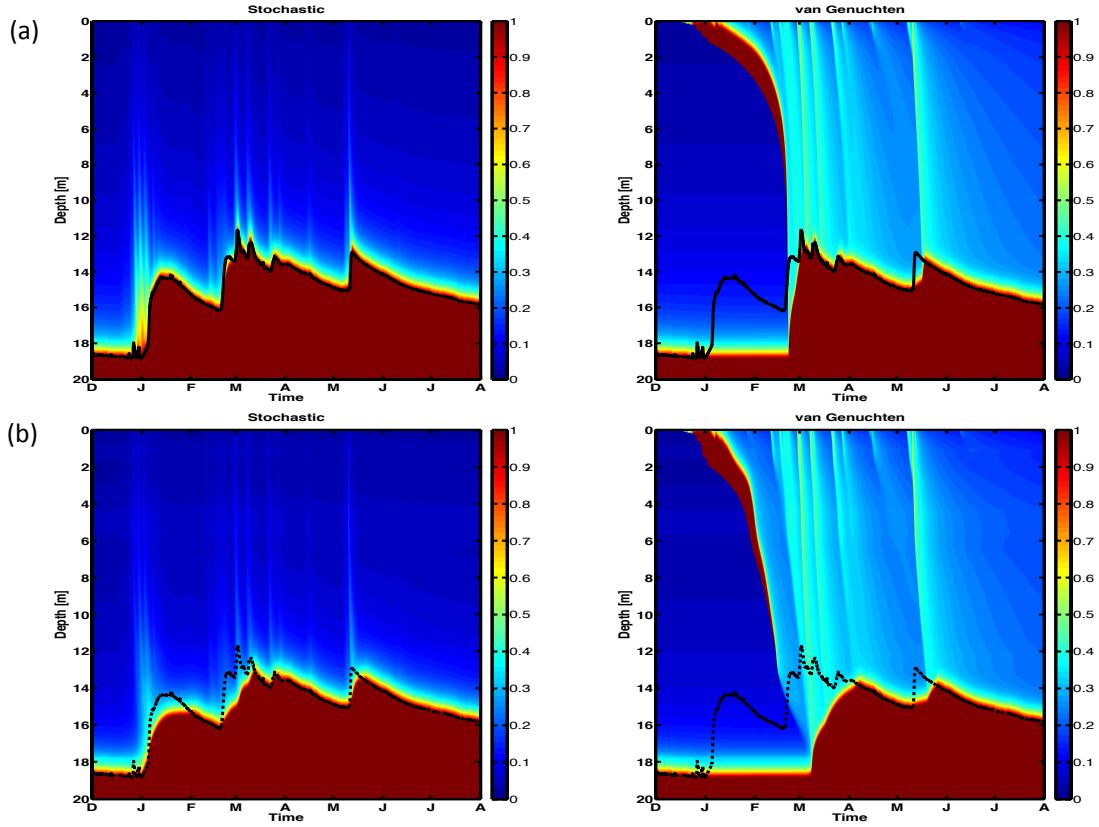

Figure 17: Effective saturation results, with (a) the stratified and (b) the noisy porosity profiles respectively. Left panel shows the ensemble mean of the new model, from 50 noise realizations. The setting for this example is $\Sigma = 2$, $\lambda = 1$. The right panel shows the corresponding results with the van Genuchten model (one model run). The vertical dimension represents the depth z [m] and the horizontal is time (in months). The black dashed line shows the observed water table depth for the whole WY:08–09.

In the example above, the stratified porosity profile demonstrates a better match of the estimated water table $z_{\hat{w}}$ with the observed one $z_{\triangledown}$. However, we must emphasize that the particular noisy profile was not chosen to match exactly the bulk porosity of the stratified one, but rather to see the effect of the choice of a non-smooth profile on the overall performance of the algorithm. We also applied different versions of noisy porosity $\theta_{\text{sat}}(z)$ where the performance, in terms of matching the observed water table, was almost identical to its (smoothed) stratified version.

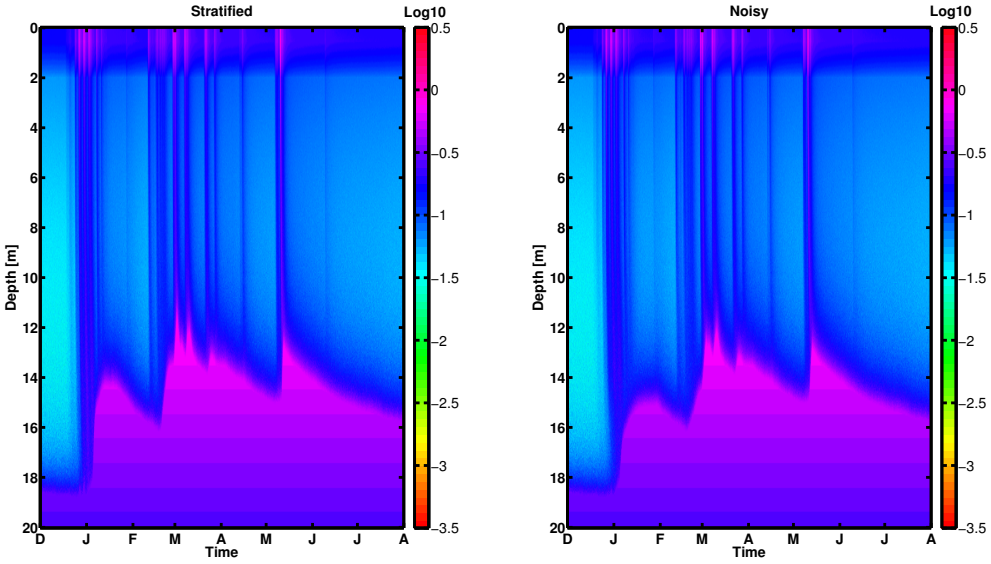

Figure 18: Ensemble mean of hydraulic conductivity $K_{stc}(\Theta)$, on logarithmic scale ($\log_{10}$), from 50 different noise realizations with the stratified (left panel) and the noisy (right panel) porosity profile. The setting for this examples is $\Sigma = 2$, $\lambda = 1$.

Likewise, the comparison between the ensemble results of the new hydraulic conductivity $K_{stc}(\Theta)$ (Eq. 10), between the two different porosity profiles, along with the random K_{bkg}, are illustrated in Figures (18) and (19) respectively. The former figure shows the average result from all simulations, whilst the later presents only one example of the K_{bkg} (out of the fifty), to emphasize its stochastic nature. It is easy to identify visually the separation of the saprolite layer, on the top of the spatial domain, from the weathered bedrock and how the results are smoothed out in the saturated zone below the estimated water table. Moreover, it is clear how high conductivity paths are formulated that allow the water to move faster from the surface to the water table.

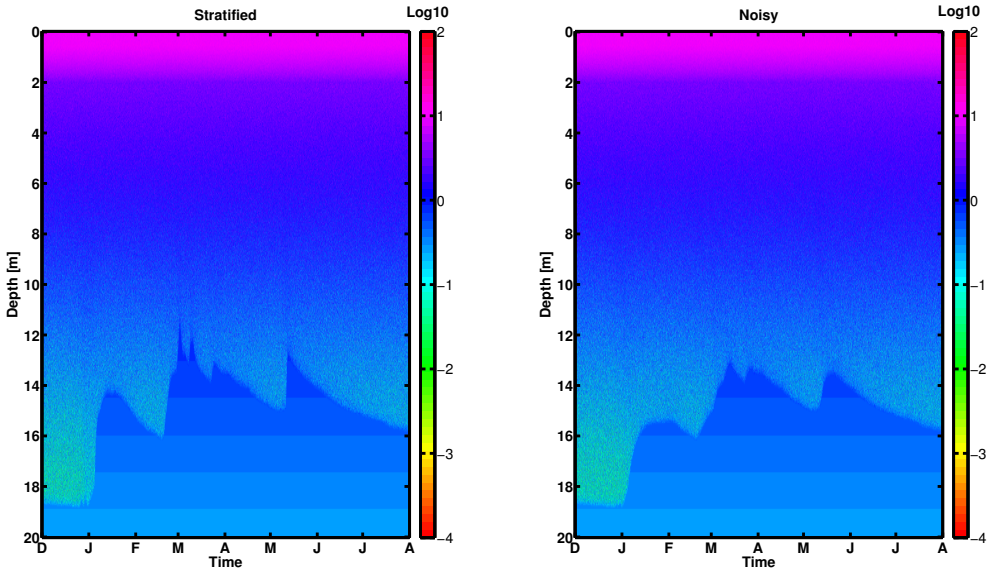

Figure 19: Hydraulic conductivity K_{bkg}, on logarithmic scale ($\log_{10}$), from a single ensemble member. The setting for this example is $\Sigma = 2$, $\lambda = 1$. Left panel shows the results with the stratified porosity, while right panel displays the results obtained with the noisy profile. Notice how the values decrease with increasing depth.

5.2.2 Runoff estimation and water storage

The excess of water that leaves the spatial domain is approximated numerically in a two step procedure as described in Section (4.4). This is a *by-product* of our algorithm that can be monitored and provide useful insight into the overall performance of the new model.

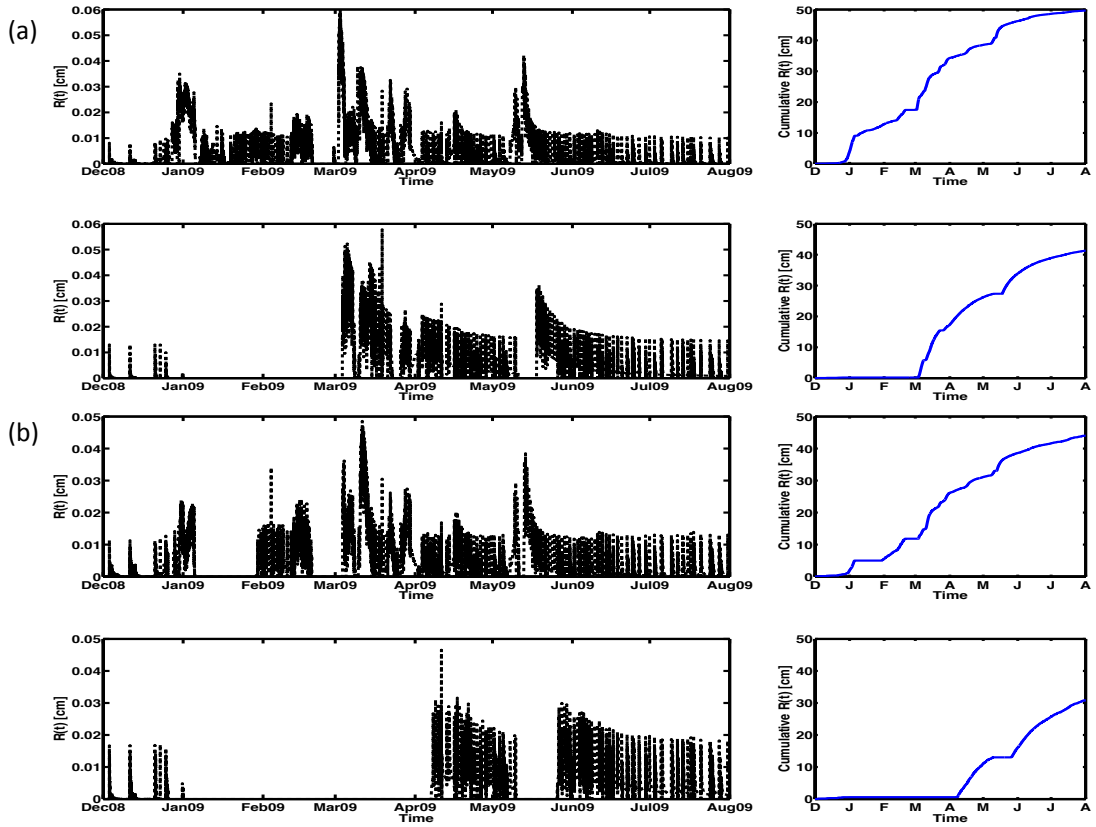

Figure 20: Runoff R(t) [cm], as a function of time, with (a) the stratified and (b) the noisy porosity profiles respectively. Left top panel (on each plot separately) shows the ensemble mean of the new model, from 50 different noise realizations, whilst the left bottom panel shows the same result with the van Genuchten model (one model run). The estimation of runoff is performed numerically, as shown in Figure (13). The right side panels (blue lines) present the corresponding cumulative runoff for the two models respectively, over the same time period.

Figure 20(a) presents the runoff results, for both models, using the same stratified porosity profile. The left side panels (plotted with black dashed lines) show the runoff in [cm] units over the whole WY:08–09, for the new stochastic model (top left) and the deterministic van Genuchten (bottom left). It is clear that since the new stochastic approach allows the water to move quickly to the lower levels in the underground that would lead to an increased runoff, as seen over the whole time domain. On the contrary, the van Genuchten model, with a few exceptions in December 2008, starts producing output only after March 2009, essentially with more than two months delay. We also observe that for the months that both models produce runoff, the van Genuchten model is slightly higher mainly due to the fact that it has more water accumulated in the unsaturated weathered bedrock area (above the water table). On the right hand side of these plots (shown with blue solid lines) are highlighted the cumulative results of both examples. As expected the new model produces more runoff, around 10cm in this example, with respect to the van Genuchten. We also note that the results presented for the stochastic approach are the ensemble mean of the fifty model runs.

In a similar manner, Figure 20(b) presents the same result but with the noisy porosity profile. Even though the results for both porosity profiles are different, the overall behavior of both models is consistent. In this case we also see a significant delay of the van Genuchten model to produce runoff and despite the fact that both models achieve less cumulative runoff, with respect to the stratified profile, the difference between the two models is almost the same (around 10cm).

However, what really captures the hydrologic conditions in the underground is highlighted in Figure 21. These plots show the time-varying partitioning of the integrated volumetric water content among the soil, saprolite, unsaturated and saturated weathered bedrock, normalized with the instantaneous total amount of water, for the two porosity profiles. The integrated volumetric water content [cm], for each of the underground layers separately, is given by:

$$\mathrm{w_U}(t) = \int_{z \in U} \theta(z,t) dz \,, \tag{21}$$

where U = {soil, saprolite, weathered–var, weathered–sat}, defines a set of four underground layers. Note that the weathered bedrock layer is divided into two zones: (a) the variably saturated zone (above the estimated water table $z_{\hat{w}}$) and (b) the fully saturated zone (below the estimated water table $z_{\hat{w}}$).

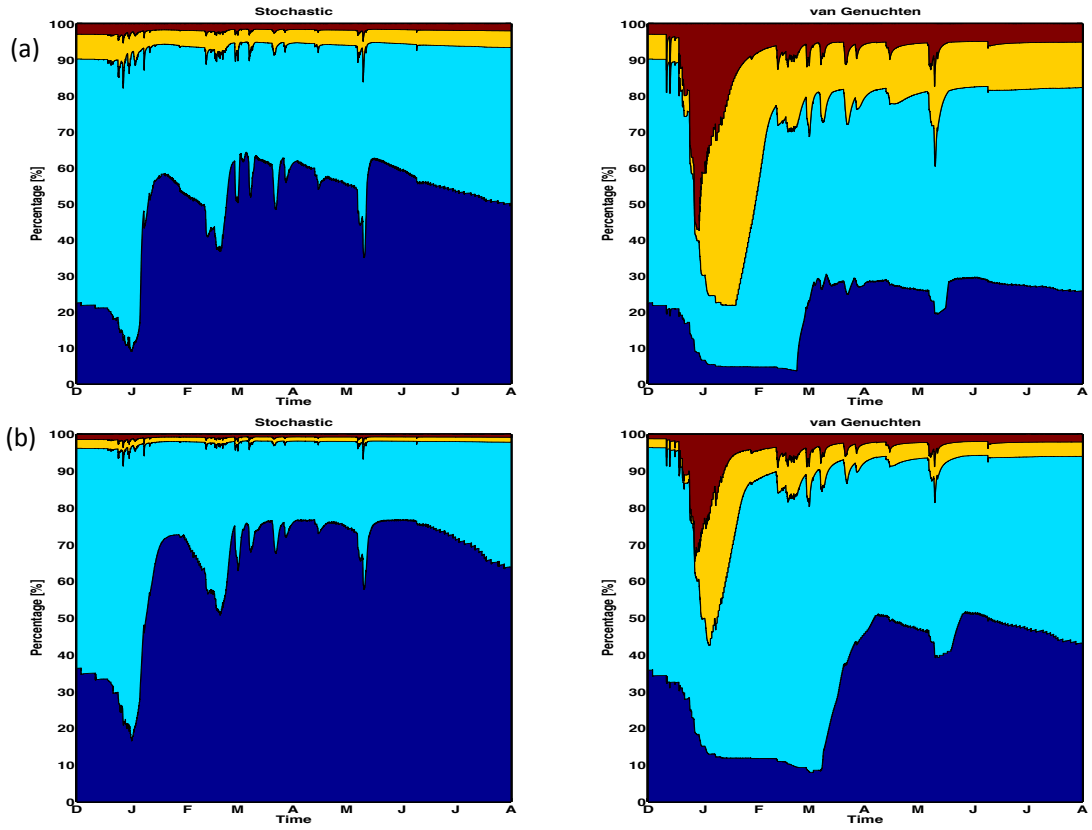

Figure 21: Percentage of water in each underground layer, with (a) the stratified and (b) the noisy porosity profiles respectively, for the two models. The left side displays the ensemble mean from 50 different noise realizations of the new model. The right panel shows the same results for the van Genuchten model. Dark blue (at the bottom) is the water in the saturated zone (below the water table), light blue is the remaining water in the weathered bedrock, yellow is the saprolite layer and with red color at the top is the water in the soil layer. The values have been normalized with the total amount of water. The parameter setting for the new model in this example is $\Sigma = 2$ and $\lambda = 1$.

It is clear that with either porosity profile, the new stochastic approach (left panels) stores less water in the zone above the water table compared to the van Genuchten (right panels). On average it stores around 40% with the stratified profile and 30% with the noisy, while the corresponding percentages with the van Genuchten approach are 70% and 55%. In fact it is obvious that during the month of January, when the new approach starts responding quickly to the first winter rains the van Genuchten model stores most of the water in the soil and saprolite areas causing saturation that is not supported by real observations.

5.2.3 Temporal variability

Finally, taking averages with respect to the time dimension [T], for the WY:08–09 period, we compute vertical (empirical) profiles of the $\theta(z,t)$, Θ and K_{rel}. Note that the relative hydraulic conductivity profile is computed as: $K_{rel} = K(\Theta)/K_{sat}$, which in the new stochastic approach translates to: $K_{rel} = K_{stc}(\Theta)/\mu(z)$.

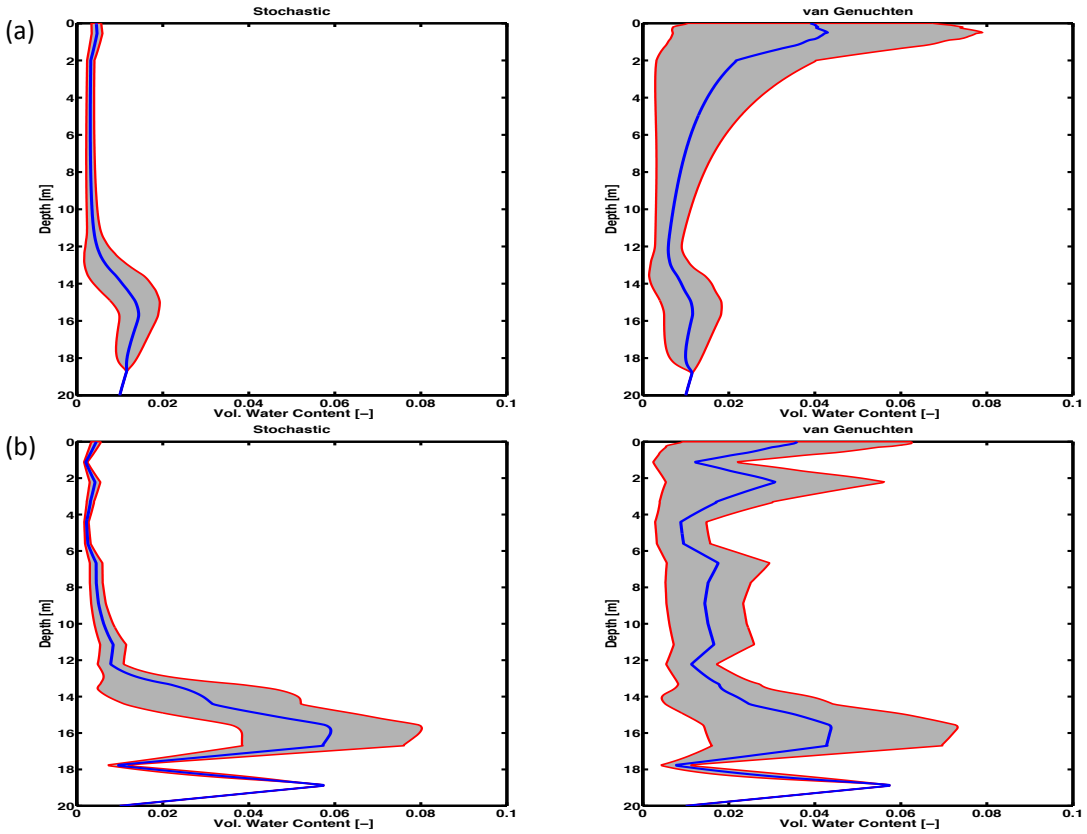

Figure 22: Temporal mean (blue line) $\pm 1 \times$ std (grey shaded area), of the volumetric water content, as function of space, with (a) the stratified and (b) the noisy porosity profiles respectively. Left panel shows the results from a single ensemble member of the new stochastic approach, while the right panel presents the same results but from a single model run of the van Genuchten model. These are computed from the estimated $\theta(z,t)$ for the period of one water year. Notice that at the bottom of the domain ($\approx$ 18.5 m and below) there is no variation (std = 0), since these locations are always saturated. The setting for the stochastic example is $\Sigma = 2$, $\lambda = 1$.

Figures 22(a) and 22(b) contrast the volumetric water content profiles for the *stratified* and *noisy* porosity functions respectively. The water table fluctuates seasonally between 12–18.5m, and so the spread in Θ is approximately the same with either the stochastic and van Genuchten approaches, but slightly higher with the later which fails to capture the early rise of the water table. It is clear that the van Genuchten approach tends to keep water in the upper soil layers, whilst both approaches are more similar between the 12–20m, where the fluctuation zone of the water table exists. In all illustrations, the vertical blue lines indicate the mean value (as function of depth z), whereas the shaded areas represent the one standard deviation. It is notable, that at the bottom of the domain the variability vanishes since our initial conditions include the water table inside the domain and this part remains saturated ($\approx$ 18.5m and below).

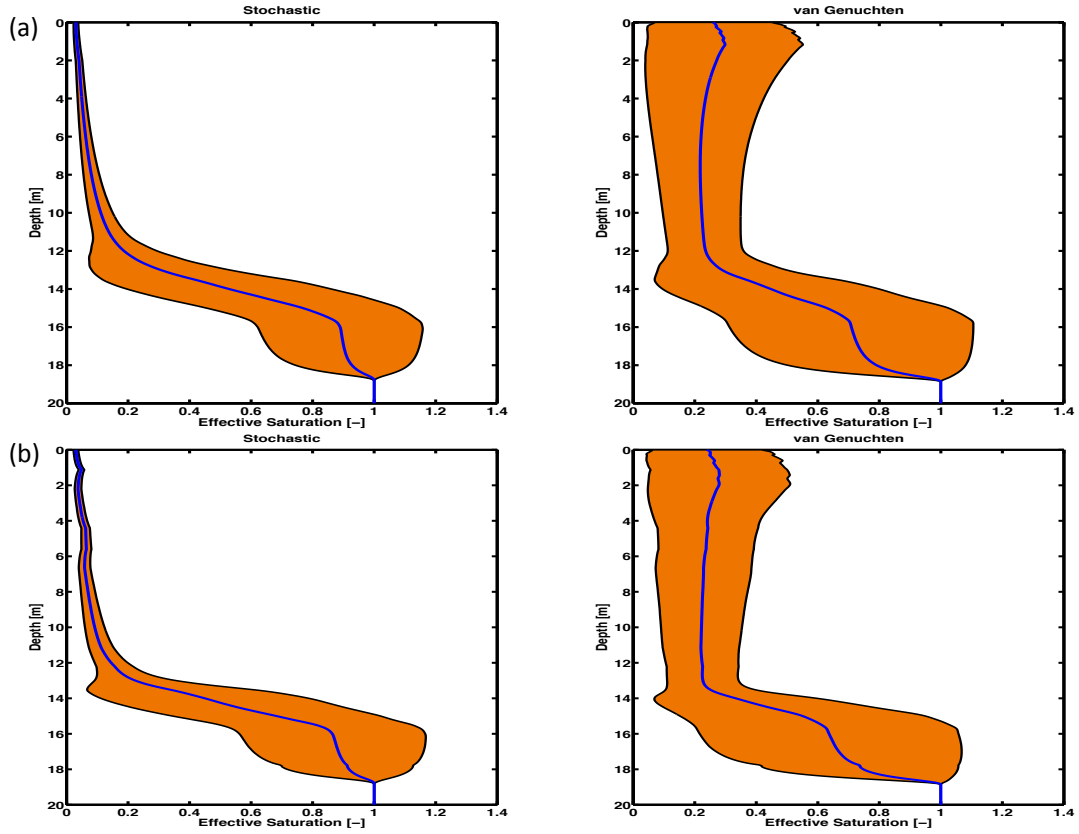

Figure 23: Temporal mean (blue line) $\pm 1 \times$ std (orange shaded area), of the effective saturation (normalized water content), as function of space with (a) the stratified and (b) the noisy porosity profiles respectively. Left panel shows the results from a single ensemble member of the new stochastic approach, while the right panel presents the same results but from a single model run of the van Genuchten model. These are computed from the estimated Θ for the period of WY:08–09. Notice that at the bottom of the domain (≈ 18.5 m and below) there is no variation (std $= 0$), since these locations are always saturated. The setting for the stochastic example is $\Sigma = 2$, $\lambda = 1$.

The same conclusion is supported from Figures 23(a) and 23(b), where the water content is normalized and the effective saturation results Θ are shown, again for the two different approaches.

Lastly, Figures 24 (a) and (b) presents the results of the relative hydraulic conductivity. It is apparent that the choice of the porosity profile does not alter significantly the total behavior of the models and has only minor effects. Clearly the van Genuchten model shows higher uncertainty in the upper layers of the soil, mainly because its stays saturated for longer periods of time, in contrast to the new stochastic approach where the water moves quicker to the lower layers.

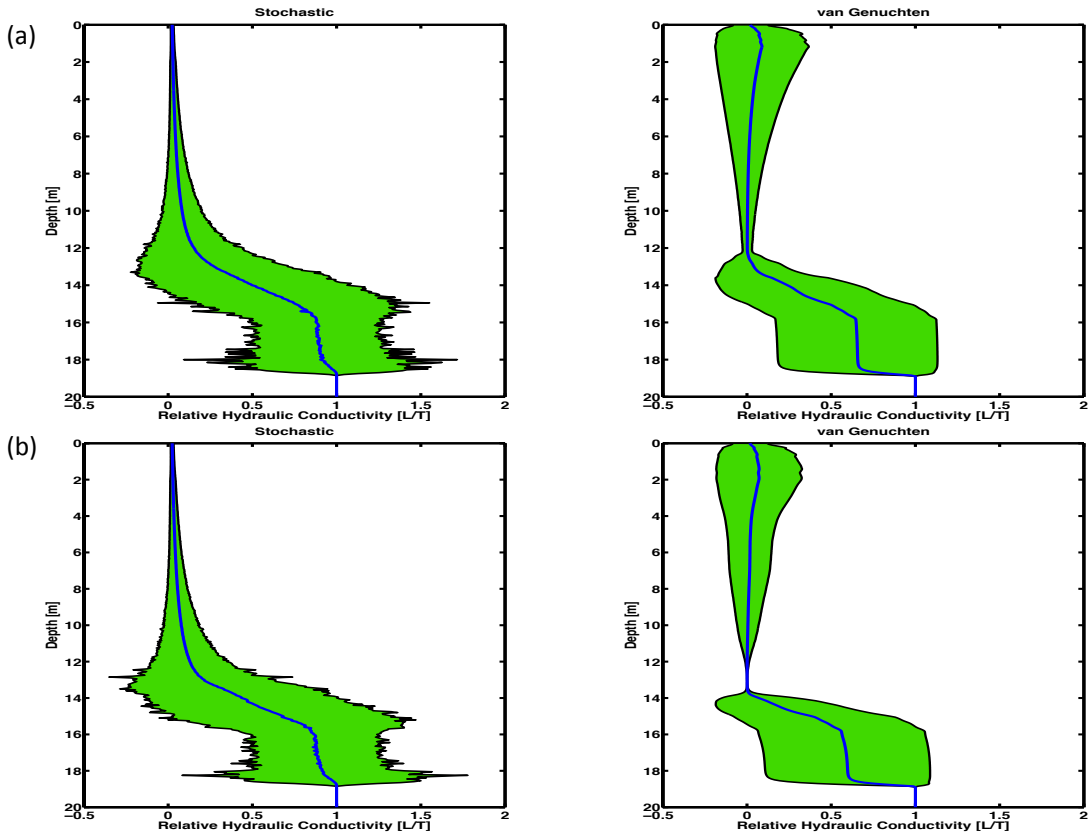

Figure 24: Temporal mean (blue line) $\pm 1 \times$ std (green shaded area), of the relative hydraulic conductivity, as function of space with (a) the stratified and (b) the noisy porosity profiles respectively. Left panel shows the results from a single ensemble member of the new stochastic approach, while the right panel presents the same results but from a single model run of the van Genuchten model. These are computed from the estimated K_{rel} for the period of WY:08–09. Notice that at the bottom of the domain ($\approx$ 18.5 m and below) there is no variation (std = 0), since these locations are always saturated. The setting for the stochastic example is $\Sigma = 2$, $\lambda = 1$.

6 Discussion

We have presented a new approach for modeling one–dimensional vertical flow in variably saturated porous media. This method posits that a naturally occurring porous medium can be better represented by a set of parameters that have a probability density function, that would account for heterogeneity of the subsurface geology and the plethora of possible flow paths. Such an approach could also capture various sources of uncertainty.

The proposed stochastic hydraulic conductivity model is simple in conception, easy in implementation and can be adapted to meet specific site characteristic, given that such prior knowledge exists. It yields an optimal representation of hydraulic conductivity as $K(\Theta) = \Theta^{\lambda} K_{bkg}$, with $\lambda = 1$. Whilst the optimal value for the noise amplitude Σ was found at 2, a range of higher Σ values was tested but the results were not significantly better, in terms of RMSE and NSC; however they came at much higher computational costs.

The model shows that the volumetric water content $\theta(z,t)$ at any depth, within the weathered bedrock, is highly variable throughout the rainy season. With a low permeability a layer saturates rapidly, which causes an increase in its hydraulic conductivity, thus facilitating the rapid downward transit of rainwater into the deeper underground layers. The weathered bedrock above the water table with its great depth, stores a significant fraction ($> 30\%$) of the total water in the column despite its low porosity. While it may be argued that the dry periods are not important for streamflow generation, the rock moisture may be a key determinant for sustaining plants through water uptake form the deep roots of the trees.

As is expected with the current stochastic formulation, $K_{stc}(\Theta)$ has a greater variance under dry

conditions. This implies great heterogeneity in Θ, in space and time, during dry conditions, thus challenging the interpretation of scant observations.

The exponentially decaying porosity profile that was chosen, unlike previous efforts [12], fixes the decay value based on the porosity at the top and the bottom of the weathered bedrock. A noisy profile, such as that inferred from the neutron probe measurements (see Figure 13 in [44]), is rarely measured. The results show that there is not much difference in the high-frequency water table response.

It is apparent that the deterministic van Genuchten model, in both examples (porosity profiles), fails to capture the quick response of the observed water table to the first winter rains and rise with delay of nearly two months. This is attributed to the fact that this hydraulic conductivity model is slow with small values of saturation in the soils, as shown in Figure (9) (right panel). Therefore, it tends to keep the water in the upper layers, causing saturation; effectively acting like a bottleneck for the rest of the soil/rock column. However, our results show that the van Genuchten model can capture the water table dynamics when wetter initial condition are used (not shown). Even so, the rock moisture would still show a rather slow wetting front, and the upper several meters of the column are too wet.

Partitioning the stored water among the soil, saprolite and weathered bedrock layers, as shown in Figure 21, the "runoff" estimated with the stochastic model is greater than the van Genuchten model as more water is held in the upper part of the soil/rock column. However, with sufficient rain we would expect that overland flow would be more likely in the van Genuchten model than in the stochastic model. That would, of course, introduce a change the top boundary condition of the RE solution Eq. (3), as the infiltration flux would exceed the maximum infiltration capacity of the surface.

We have experimented with several configurations of the mean function $\mu(z)$ (i.e. $\mathrm{K}_{\mathrm{sat}}^{\mathrm{soil}}, \mathrm{K}_{\mathrm{sat}}^{\mathrm{sap}}$ and $\mathrm{K}_{\mathrm{sat}}^{\mathrm{frs}}$ parameters) and we acknowledge that it has a significant effect to the results, of this proposed model. It is our intention to further explore its impact by using data assimilation techniques, such as the Ensemble Kalman Filter (EnKF) [10], to estimate its parameters in a more principled way. Moreover, we will explore the generalization of the new approach to different well locations, at the same research site, as well as different water years, to see if the parameters are widely applicable. We do expect the model to depend on the local geology, however since it is easy to change its parameterization we would anticipate that after careful tuning to perform satisfactory.

Acknowledgement

We thank Daniella Rempe and William Dietrich, from the EPS department of UC Berkeley, for helpful comments and discussion. This work is funded by the NSF, Mathematics and Climate Research Network (DMS-0940272) and the Department of Energy (DE-SC0010857). Part of this research used computational resources of the National Energy Research Scientific Computing center (DE-AC02-05CH11231).

A Sampling $\mathrm{K}_{\mathrm{bkg}}$ from a Log–Normal density function

Equation (10), prescribes a $\mathrm{K}_{\mathrm{bkg}}$ value that is drawn from a Log–Normal distribution with parameters ν and Λ. However, we want the random variables to have specific mean and variance functions given by Equations (12) and (13), respectively. To do that we need to define the location (ν) and scale (Λ) parameters, on the logarithmic scale, as follows:

$$\nu = \ln\left(\frac{\mu(z)^2}{\sqrt{\Sigma(1-\Theta)+\mu(z)^2}}\right), \qquad \text{and} \tag{22}$$

$$\Lambda = \sqrt{\ln\left(\frac{\Sigma(1-\Theta)}{\mu(z)^2}+1\right)}. \tag{23}$$

Therefore $\mathrm{K}_{\mathrm{bkg}}(z,\Theta) = \exp\{\nu + \Lambda\epsilon_z\}$, with $\epsilon_z \sim \mathrm{N}(0,1)$. Note that the dependence of $\mathrm{K}_{\mathrm{bkg}}$ on depth z and effective saturation Θ is now made explicit, to emphasize that different random variables are drawn for each location.

A.1 Proof of $\langle \mathbf{K_{bkg}} \rangle$

The mean of K_{bkg} is given by:

$$\begin{aligned}
\langle K_{bkg} \rangle &= \exp\left\{\nu + \frac{1}{2}\Lambda^2\right\} \\
&= \exp\left\{ \ln\left(\frac{\mu(z)^2}{\sqrt{\Sigma(1-\Theta)+\mu(z)^2}}\right) + \right. \\
&\qquad \left. \frac{1}{2}\ln\left(\frac{\Sigma(1-\Theta)}{\mu(z)^2}+1\right)\right\} \\
&= \left(\frac{\mu(z)^2}{\sqrt{\Sigma(1-\Theta)+\mu(z)^2}}\right)\sqrt{\left(\frac{\Sigma(1-\Theta)}{\mu(z)^2}+1\right)} \\
&= \frac{\mu(z)^2}{\sqrt{\Sigma(1-\Theta)+\mu(z)^2}}\frac{\sqrt{\Sigma(1-\Theta)+\mu(z)^2}}{\mu(z)} \\
&= \mu(z)\,. \qquad (24)
\end{aligned}$$

In a similar manner it can be proven that the variance of K_{bkg} is given by $\Sigma(1-\Theta)$.

B Notation

Name	Description	Units
D	number of discrete cels	[-]
L	length	cm
T	time	0.5 hr
z	vertical dimension (depth)	[L]
t	time dimension	[T]
$\psi(z,t)$	pressure suction	[L]
$\theta(z,t)$	volumetric water content	$[L^3/L^3]$
$\theta_{sat}(z)$	volumetric water content at saturation	$[L^3/L^3]$
θ_{res}	residual volumetric water content	$[L^3/L^3]$
θ_{min}	minimum volumetric water content	$[L^3/L^3]$
θ_{max}	maximum volumetric water content	$[L^3/L^3]$
Θ	effective saturation	$[L^3/L^3]$
$K(\Theta)$	hydraulic conductivity (unsaturated)	[L/T]
K_{sat}	hydraulic conductivity (saturated)	[L/T]
$C(\psi)$	specific moisture capacity	[1/L]
$S(z,\psi)$	sink term	[1/T]
$N(m,Q)$	Normal distribution with mean m and (co)-variance Q	[-]
$LogN(\nu,\Lambda)$	Log-Normal distribution with parameters ν and Λ	[-]
RMSE	Root mean square error	[L]
NS	Nash–Sutcliffe statistic	[-]

References

[1] B. Berkowitz, J. Klafter, R. Metzler, and H. Scher. Physical pictures of transport in heterogeneous media advection dispersion random walk and fractional derivative formulations. *Water Resources Research*, 38(10):1–12, 2002.

[2] C. A. Brebbia and S. Walker. *Boundary element techniques in engineering*, volume 980. Newnes-Butterworths London, 1980.

[3] K. J. Brust, C. H. M. van Bavel, and G. B. Stirk. Hydraulic Properties of a Clay Loam Soil and the Field Measurement of Water Uptake by Roots: III. Comparison of Field and Laboratory Data on Retention and of Measured and Calculated Conductivities. *Soil Science Society of America Journal*, 32(3):322–326, May 1968.

[4] W. Brutsaert. *Hydrology: An Introduction*. Cambridge University Press, 2005.

[5] G. L. Butters and P. Duchateau. Continuous Flow Method for Rapid Measurement of Soil Hydraulic Properties: I. Experimental Considerations. *Vadose Zone Journal*, 1(0):239–251, April 2002.

[6] M. A. Celia, E. T. Bouloutas, and R. L. Zarba. A General Mass-Conservative Numerical Solution for the Unsaturated Flow Equation. *Water Resources Research*, 26(7):1483–1496, July 1990.

[7] T. P. Clement, W. R. Wise, and F. J. Molz. A physically based, two-dimensional, finite-difference algorithm for modeling variably saturated flow. *Journal of Hydrology*, 161(0):71–90, March 1994.

[8] G. Dagan. Solute transport in heterogeneous porous formations. *Journal of Fluid Mechanics*, 145(0):151–177, March 1984.

[9] J. P. Delhomme. Spatial Variability and Uncertainty in Groundwater Flow Parameters: A Geostatistical Approach. *Water Resources Research*, 15(2):269–280, April 1979.

[10] G. Evensen. The Ensemble Kalman Filter: theoretical formulation and practical implementation. *Ocean Dynamics*, 53(4):343–367, May 2003.

[11] R. Eymard, M. Gutnic, and D. Hilhorst. The finite volume method for Richards equation. *Computational Geosciences*, 3(0):259–294, September 1999.

[12] Y. Fan, G. Miguez-Macho, C. P. Weaver, R. Walko, and A. Robock. Incorporating water table dynamics in climate modeling: 1. water table observations and equilibrium water table simulations. *Journal of Geophysical Research*, 112(D10125):1–17, May 2007.

[13] X. Foussereau, W. D. Graham, and P. S. C. Rao. Stochastic analysis of transient flow in unsaturated heterogeneous soils. *Water Resources Research*, 36(4):891–910, April 2000.

[14] R. A. Freeze. A stochastic-conceptual analysis of one-dimensional groundwater flow in nonuniform homogeneous media. *Water Resources Research*, 11(5):725–741, 1975.

[15] R. A. Freeze. The role of stochastic hydrogeological modeling in real-world engineering applications. *Stochastic Environmental Research and Risk Assessment*, 18(0):286–289, 2004.

[16] L. W. Gelhar. Stochastic subsurface hydrology from theory to applications. *Water Resources Research*, 22(9):135–145, August 1986.

[17] H. H. Gerke and M. T. van Genuchten. A Dual-Porosity Model for Simulating the preferential Movement of Water and Solutes in Structured Porous Media. *Water Resources Research*, 29(2):305–319, February 1993.

[18] R. Haverkamp, M. Vauclin, J. Touma, P. J. Wierenga, and G. Vachaud. A comparison of numerical simulation models for one-dimensional infiltration. *Soil Science Society of America*, 41(0):285–295, January 1977.

[19] J. W. Hopmans, J. R. Šimunek, N. Romano, and W. Durner. *Methods of soil analysis*, volume 4 of *5*, chapter Inverse methods, pages 963–1008. SSSA, Madison, WI, 2002.

[20] U. Hornung and W. Messing. Simulation of two-dimensional saturated/unsaturated flows with an exact water balance. *Flow and transport in porous media*, pages 91–96, 1981.

[21] S. K. Kampf and S. J. Burges. A framework for classifying and comparing distributed hillslope and catchment hydrologic models. *Water Resources Research*, 43(W05423):1–24, May 2007.

[22] J. Law. A Statistical Approach to the Interstitial Heterogeneity of Sand Reservoirs. *Transactions of the AIME*, 155(01):202–222, December 1944.

[23] D. M. Lawrence, K. W. Oleson, M. G. Flanner, P. E. Thornton, S. C. Swenson, P. J. Lawrence, X. Zeng, Z.-L. Yang, S. Levis, K. Sakaguchi, G. B. Bonan, and A. G. Slater. Parameterization improvements and functional and structural advances in version 4 of the community land model. *Journal of Advances in Modelling Earth Systems*, 3(2011MS000045):1–27, March 2011.

[24] C. T. Miller, C. Abhishek, and M. W. Farthing. A spatially and temporally adaptive solution of richards' equation. *Advances in Water Resources*, 29(0):525–545, December 2006.

[25] C. T. Miller, G. A. Williams, C. T. Kelley, and M. D. Tocci. Robust solution of Richards' equation for non-uniform porous media. *Water Resources Research*, 34(10):2599–2610, 1998.

[26] P. C. D. Milly. A mass-conservative procedure for time-stepping in models of unsaturated flow. *Advanced Water Resources*, 8:32–36, March 1985.

[27] Y. Mualem. A new model for predicting the hydraulic conductivity of unsaturated porous media. *Water Resources Research*, 12(3):513–523, July 1976.

[28] J. E. Nash and J. V. Sutcliffe. River flow forecasting through conceptual models part I – A discussion of principles. *Journal of Hydrology*, 10(3):282–290, 1970.

[29] S. P. Neuman. Saturated-unsaturated seepage by finite elements. *Journal of the hydraulics division*, 99(12):2233–2250, December 1973.

[30] J. R. Nimmo. Theory for source-responsive and free-surface film modeling of unsaturated flow. *Vadose Zone Journal*, 9(0):295–306, May 2010.

[31] G.-Y. Niu, Z.-L. Yang, R. E. Dickinson, and L. E. Gulden. A simple TOPMODEL-based runoff parameterization (SIMTOP) for use in global climate models. *Journal of Geophysical Research*, 110(D21106):1–15, 2005.

[32] G.-Y. Niu, Z.-L. Yang, R. E. Dickinson, and L. E. Gulden. Development of a simple groundwater model for use in climate models and evaluation with gravity recovery and climate experiment data. *Journal of Geophysical Research*, 112(D07103):1–14, 2007.

[33] K. W. Oleson, D. M. Lawrence, G. B. Bonan, B. Drewniak, M. Huang, C. D. Koven, S. Levis, F. Li, W. J. Riley, Z. M. Subin, S. C. Swenson, and P. E. Thornton. Technical description of version 4.5 of the community land model (CLM). NCAR Technical Note NCAR/TN-503+STR, National Center for Atmospheric Research (NCAR), July 2013.

[34] L. Pan, A. W. Warrick, and P. J. Wierenga. Finite element methods for modeling water flow in variably saturated porous media: Numerical oscillation and mass-distributed schemes. *Water Resources Research*, 32(6):1883–1889, June 1996.

[35] D. Pokrajac. A Numerical Model of a Saturated-Unsaturated Porous Flow System. *Water Resources Managment*, 2(0):183–190, July 1988.

[36] M. A. Pour, M. M. Shoshtari, and A. Adib. Numerical solution of richards equation by using of finite volume method. *World Applied Sciences Journal*, 14(12):1838–1842, January 2011.

[37] G. J. Redinger, G. S. Campbell, K. E. Saxton, and R. I. Papendick. Infiltration rate of slot mulches: Measurement and numerical simulation. *Soil Science Society of America Journal*, 48(5):982–986, 1984.

[38] P. Renard. Stochastic hydrogeology: What professionals really need? *Ground Water*, 45(5):531–541, October 2007.

[39] L. A. Richards. Capillary conduction of liquids through porous mediums. *Physics*, 1(0):318–333, November 1931.

[40] P. J. Ross. Efficient numerical methods for infiltration using Richards' equation. *Water Resources Research*, 26(2):279–290, 1990.

[41] P. J. Ross. Modeling Soil Water and Solute Transport - Fast, Simplified Numerical Solutions. *Agronomy Journal*, 95(0):1352–1361, November 2003.

[42] Y. Rubin. *Applied Stochastic Hydrogeology*. Oxford University Press, March 2003.

[43] Y. Rubin. Stochastic hydrogeology - challenges and misconceptions. *Stochastic Environmental Research and Risk Assessment*, 18(0):280–281, 2004.

[44] R. Salve, D. M. Rempe, and W. E. Dietrich. Rain, rock moisture dynamics, and the rapid response of perched groundwater in weathered, fractured argillite underlying a steep hillslope. *Water Resources Research*, 48(W11528):1–25, November 2012.

[45] M. G. Schaap and M. T. van Genuchten. A Modified Mualem-van Genuchten Formulation for Improved Description of the Hydraulic Conductivity Near Saturation. *Vadose Zone Journal*, 5(0):27–34, December 2006.

[46] W. E. Schiesser. *The Numerical Method of Lines: Integration of Partial Differential Equations*. Academic Press, 3 edition, 1991.

[47] W. E. Schiesser and G. W. Griffiths. *A Compendium of Partial Differential Equation Models: Method of Lines Analysis with MATLAB*. Cambridge University Press, New York, NY, USA, 1 edition, 2009.

[48] J. Šimunek, N. J. Jarvis, M. T. van Genuchten, and A. Gardenas. Review and comparison of models for describing non equilibrium and preferential flow and transport in the vadose zone. *Journal of Hydrology*, 272(0):14–35, April 2003.

[49] J. Šimunek, O. Wendroth, and M. T. van Genuchten. Estimating unsaturated soil hydraulic properties from laboratory tension disc infiltrometer experiments. *Water Resources Research*, 35(10):2965–2979, October 1999.

[50] J. R. Šimunek, R. Kodešova, M. M. Gribb, and M. T. van Genuchten. Estimating hysteresis in the soil water retention function from cone permeameter experiments. *Water Resources Research*, 35(5):1329–1345, May 1999.

[51] R. D. Skeel and M. Berzins. A method for the spatial discretization of parabolic equations in one dimension. *Journal on Scientific and Statistical Computing, SIAM*, 11(1):1–32, 1990.

[52] M. D. Tocci, C. T. Kelley, and C. T. Miller. Accurate and economical solution of the pressure-head form of Richards' equation by the method of lines. *Advances in Water Resources*, 20(1):1–14, January 1997.

[53] M. T. van Genuchten. A closed-form equation for predicting the hydraulic conductivity of unsaturated soils. *Soil Science Society of America*, 44(5):1–8, October 1980.

[54] M. T. van Genuchten, F. J. Leij, and S. R. Yates. The RETC Code for Quantifying the Hydraulic Functions of Unsaturated Soils. Technical Report EPA/600/2-91/065, EPA, December 1991.

[55] M. J. Vepraskas, C. B. Craft, and J. L. Richardson. *Wetland Soils: Genesis, Hydrology, Landscapes and Classification*. CRC Press, 2002.

[56] J. E. Warren, F. F. Skiba, and H. S. Price. An Evaluation of the Significance of Permeability Measurements. *Journal of Petroleum Technology*, 13(08):739–744, August 1961.

[57] G. A. Williams and C. T. Miller. An evaluation of temporally adaptive transformation approaches for solving richards' equation. *Advances in Water Resources*, 22(8):831–840, November 1999.

[58] C. L. Winter. Stochastic hydrology: practical alternatives exist. *Stochastic Environmental Research and Risk Assessment*, 18(0):271–273, 2004.

[59] S. R. Yates, M. T. van Genuchten, A. W. Warrick, and F. J. Leij. Analysis of Measured, Predicted and Estimated Hydraulic Conductivity Using the RETC Computer Program. *Soil Science Society of America*, 56(0):347–354, September 1992.

[60] K. S. Zadeh. A mass-conservative switching algorithm for modeling fluid flow in variably saturated porous media. *Journal of Computational Physics*, 230:664–679, 2011.

[61] X. Zeng and M. Decker. Improving the numerical solution of soil moisture-based richards equation for land models with a deep or shallow water table. *Journal of Hydrometeorology*, 10(0):308–319, February 2009.

[62] O. C. Zienkiewicz and C. J. Parekh. Transient field problems: Two-dimensional and three-dimensional analysis by isoparametric finite elements. *International Journal for Numerical Methods in Engineering*, 2(1):61–71, 1970.